Pergamon

Geochimica et Cosmochimica Acta, Vol. 68, No. 8, pp. 1857–1887, 2004

0016-7037/04 $30.00 + .00

doi:10.1016/j.gca.2003.10.021

Zircon (U-Th)/He thermochronometry: He diffusion and comparisons with $^{40}Ar/^{39}Ar$ dating

PETER W. REINERS,[1,*] TERRY L. SPELL,[2] STEFAN NICOLESCU,[1] and KATHLEEN A. ZANETTI[2]

[1]Department of Geology and Geophysics, Yale University, New Haven, CT 06511, USA
[2]Department of Geoscience, University of Nevada, Las Vegas, Las Vegas, NV 89154, USA

(*Received May* 22, 2003; *accepted in revised form October* 20, 2003)

Abstract—(U-Th)/He chronometry of zircon has a wide range of potential applications including thermochronometry, provided the temperature sensitivity (e.g., closure temperature) of the system be accurately constrained. We have examined the characteristics of He loss from zircon in a series of step-heating diffusion experiments, and compared zircon (U-Th)/He ages with other thermochronometric constraints from plutonic rocks. Diffusion experiments on zircons with varying ages and U-Th contents yield Arrhenius relationships which, after about 5% He release, indicate E_a = 163–173 kJ/mol (39–41 kcal/mol), and D_0 = 0.09–1.5 cm^2/s, with an average E_a of 169 ± 3.8 kJ/mol (40.4 ± 0.9 kcal/mol) and average D_0 of $0.46^{+0.87}_{-0.30}$ cm^2/s. The experiments also suggest a correspondence between diffusion domain size and grain size. For effective grain radius of 60 μm and cooling rate of 10°C/myr, the diffusion data yield closure temperatures, T_c, of 171–196°C, with an average of 183°C. The early stages of step heating experiments show complications in the form of decreasing apparent diffusivity with successive heating steps, but these are essentially absent in later stages, after about 5–10% He release. These effects are independent of radiation dosage and are also unlikely to be due to intracrystalline He zonation. Regardless of the physical origin, this non-Arrhenius behavior is similar to predictions based on degassing of multiple diffusion domains, with only a small proportion (<2–4%) of gas residing in domains with a lower diffusivity than the bulk zircon crystal. Thus the features of zircon responsible for these non-Arrhenius trends in the early stages of diffusion experiments would have a negligible effect on the bulk thermal sensitivity and closure temperature of a zircon crystal.

We have also measured single-grain zircon (U-Th)/He ages and obtained $^{40}Ar/^{39}Ar$ ages for several minerals, including K-feldspar, for a suite of slowly cooled samples with other thermochronologic constraints. Zircon He ages from most samples have 1 σ reproducibilities of about 1–5%, and agree well with K-feldspar $^{40}Ar/^{39}Ar$ multidomain cooling models for sample-specific closure temperatures (170–189°C). One sample has a relatively poor reproducibility of ~24%, however, and a mean that falls to older ages than predicted by the K-feldspar model. Microimaging shows that trace element zonation of a variety of styles is most pronounced in this sample, which probably leads to poor reproducibility via inaccurate α-ejection corrections. We present preliminary results of a new method for characterizing U-Th zonation in dated grains by laser-ablation, which significantly improves zircon He age accuracy.

In summary, the zircon (U-Th)/He thermochronometer has a closure temperature of 170–190°C for typical plutonic cooling rates and crystal sizes, it is not significantly affected by radiation damage except in relatively rare cases of high radiation dosage with long-term low-temperature histories, and most ages agree well with constraints provided by K-spar $^{40}Ar/^{39}Ar$ cooling models. In some cases, intracrystalline U-Th zonation can result in inaccurate ages, but depth-profiling characterization of zonation in dated grains can significantly improve accuracy and precision of single-grain ages.

1. INTRODUCTION

Zircon has a number of advantages as a suitable mineral for geochronology, including its resistance to physical and chemical weathering, relatively high abundance in a wide range of rock types, and high U-Th concentrations. U/Pb dating of zircon is the most commonly used technique for constraining high-temperature (i.e., crystallization or high-grade metamorphism) ages of rocks, and recent advances in microanalytical techniques have augmented the ability to obtain concordant and easily interpretable ages. The same decay chains that produce radiogenic Pb in zircon also produce radiogenic He, though the utility of zircon (U-Th)/He dating has received much less attention until recently.

In this study, we further characterize the temperature sensitivity of the zircon (U-Th)/He system for use in thermochronometry and outline salient technical aspects and challenges in zircon He dating. We present results and interpretations of laboratory He diffusion experiments and comparisons between zircon He ages and thermal histories derived from other isotopic dating systems. This study examines complexities in He diffusion in zircon seen in a previous study (Reiners et al., 2002a), but here we show that these effects are likely insignificant for the bulk closure temperature of the zircon (U-Th)/He system, which is ~170–190°C for typical plutonic cooling histories. We also show that zircon He ages generally agree well with K-feldspar $^{40}Ar/^{39}Ar$ cooling models, but that exceptions exist which are likely related to intracrystalline U-Th zonation.

1.1. Zircon He and K-feldspar Ar Comparisons

Based on previous diffusion experiments (Reiners et al., 2002a) and interchronometer calibrations (Kirby et al., 2002;

* Author to whom correspondence should be addressed (peter.reiners@yale.edu).

Reiners et al., 2003), the inferred temperature sensitivity of the zircon (U-Th)/He system overlaps with that of the low-temperature part of most K-feldspar $^{40}Ar/^{39}Ar$ cooling curves derived from multidomain diffusion modeling (Lovera et al., 1989, 1991, 2002; Richter et al., 1991; McDougall and Harrison, 1999). Thus, in comparing zircon (U-Th)/He ages to thermal history constraints from other systems, we have relied largely on K-feldspar $^{40}Ar/^{39}Ar$ cooling models to "check" zircon He ages. Several authors have attempted to call into question some of the assumptions of K-feldspar $^{40}Ar/^{39}Ar$ multidomain cooling models (Parsons et al., 1999; Reddy et al., 2001; Villa, 1994; Arnaud and Kelley, 1997). These authors commonly focus on issues of correspondence between assumed configuration of Ar diffusion domains and pathways in K-feldspar (as represented by mathematics required for deconvolving cooling paths), and their actual physical configurations (Fitzgerald and Harrison, 1993; Arnaud and Kelley, 1997), as well as the effects of low-temperature recrystallization. However, several studies (e.g., McDougall and Harrison, 1999; Lovera et al., 2002) have pointed out that the actual physical correspondence of K-feldspar structures to theoretical diffusion domains as represented in multidomain models is not particularly relevant, as a wide range of configurations lead to mathematically similar results that would produce essentially the same cooling history model. Lovera et al. (2002) have emphasized that the critical test of viability of the multidomain diffusion cooling-model approach (including the effects of low-T recrystallization) is simply good correspondence, during laboratory step heating, between changes in Ar diffusion characteristics and $^{40}Ar/^{39}Ar$ step-heating age spectra. Good correlations, quantified by Lovera et al.'s C_{fg} parameter, are exhibited by most dated samples, and this can easily be used to screen out suspect samples. There is also a large and growing database of K-feldspar cooling models combined with other thermochronologic and geologic constraints which can be used to empirically assess accurate calibration and underlying assumptions of techniques; these studies largely support K-feldspar $^{40}Ar/^{39}Ar$ models and their fundamental bases.

Although beyond the scope of this study, the typically overlapping thermal sensitivities of the zircon (U-Th)/He and K-feldspar $^{40}Ar/^{39}Ar$ systems may allow future comparisons or cross-calibrations of these two techniques with very different systematics and assumptions. If the thermal sensitivity of the zircon (U-Th)/He system can be confidently constrained, it may in fact provide most rigorous comparisons with K-feldspar $^{40}Ar/^{39}Ar$ results. Although titanite and zircon fission-track systems are thought to have effective closure temperatures higher than that for He in zircon, and somewhere in the intermediate or higher-temperature portions of K-feldspar cooling models, few studies have attempted detailed comparisons of results of either of these systems with those from K-feldspar $^{40}Ar/^{39}Ar$. Further, at least for zircon fission-track there is a relatively wide range of estimates for effective closure temperature and uncertainty regarding the potential influence of radiation damage in natural samples (Harrison et al., 1979; Zaun and Wagner, 1985; Hurford, 1986; Tagami et al., 1990; Brandon and Vance, 1992; Yamada et al., 1995; Foster et al., 1996; Tagami et al., 1998).

1.2. Previous Work

Strutt (1910a,b) was the first to date zircon using the (U-Th)/He system. He obtained ages ranging from 0.1 Ma to 565 Ma for zircons from Mt. Vesuvius and Ontario, respectively. Strutt recognized that He ages were, in general, "minimum values, because He leaks out from the mineral, to what extent it is impossible to say" (Strutt, 1910c). But similar to other early attempts with other minerals and isotopic systems, Strutt's work did not recognize the potential that He "leakage" could be understood as a systematic, thermally activated process, and the potential for this in thermochronometry.

In the case of zircon as well as titanite, He "leakage" was often considered to be the result of escape of gas aided by radiation-damaged zones of the crystal. Detailed work on the relationship between He age and radiation dosage was done in the 1950s by Hurley and coworkers (Hurley, 1952; Hurley and Fairbairn, 1953; Hurley et al., 1956), in which they observed correlations between damage and apparent He loss since formation. However, Damon and Kulp (1957) concluded that radiation damage could not be the only reason for zircon He ages that were less than formation ages.

Modern perspectives on thermochronometry emphasize the importance of thermal history and sample diffusion properties in producing measured ages younger than formation ages, especially for the K-Ar (Harper, 1973; McDougall and Harrison, 1999), fission-track (Gallagher et al., 1998), and (U-Th)/He systems (Zeitler et al., 1987; Wolf et al., 1996, 1998), but also for other higher-temperature systems. Zeitler et al. (1987) were the first to propose thermochronometric use of the (U-Th)/He system, specifically for apatite. Subsequent development of the interpretational bases and analytical techniques for He dating of apatite (Wolf et al., 1996; Farley et al., 1996; Farley, 2000) and titanite (Reiners and Farley, 1999) motivated work on zircon (U-Th)/He dating in the context of thermochronometry (Reiners et al., 2002a).

Reiners et al. (2002a) presented zircon (U-Th)/He ages from the rapidly cooled Fish Canyon Tuff that agreed with ages determined by other techniques; Tagami et al. (2003) also dated a suite of rapidly cooled zircons, with generally good results except for one sample with apparently extreme intracrystalline U-Th zonation. Reiners et al. (2002a) presented zircon He ages from a transect through a formerly steeply-dipping crustal section in the Basin and Range which, combined with other themochronometric constraints, suggested a closure temperature for the zircon (U-Th)/He system of approximately 200°C. This study also presented step-heating diffusion experiment results for zircon, which suggested an approximate closure temperature for the zircon He system of 180–200°C. These diffusion experiments showed complexities to the Arrhenius plots in the form of progressive changes in the apparent diffusion characteristics during early stages of the experiments, with increasing frequency factors (D_0/a^2) and activation energies (E_a), the latter in the range of 126–184 kJ/mol (30–44 kcal/mol). Assuming that diffusion characteristics determined from the early stages of these step-heating experiments represented effects arising from radiation damage or second-order complications such as inhomogeneous He distribution, cracks, or grain-size variations, the later portions of these experiments were used to suggest E_a of approximately 147–184 kJ/mol

(35–44 kcal/mol), and closure temperatures of 144–190°C (for a cooling rate of 10°C/myr).

A few studies have measured zircon He ages on samples for which thermal history constraints from other systems are also available (Kirby et al., 2002; Reiners et al., 2002b, 2003). Comparisons with K-feldspar $^{40}Ar/^{39}Ar$ and fission-track constraints in these cases suggest closure temperatures for the zircon He system in the range of 160–200°C. Nasdala et al. (2004) reported (U-Th)/He ages of detrital zircons from Sri Lanka (also studied by Hurley et al., 1956), and compared these with zircon (U-Th)/Pb, garnet Sm/Nd, and biotite Rb/Sr ages of related samples. Zircon He ages of these samples are similar to those of biotite Rb/Sr ages, which may suggest a higher closure temperature, around 250–300°C. Such high closure temperatures would be expected for the extremely large grain sizes (~1 cm diameter) of these zircons, if the effective diffusion domain for zircon is the grain size, as in the case of apatite and titanite (Reiners and Farley, 1999; Farley, 2000; Reiners and Farley, 2001). Results of this study also suggested that in a subset of these grains, radiation damage significantly increased He diffusion and compromised (U-Th)/He ages; zircons in this subset had experienced atypically high radiation dosages ($>\sim 2-4 \times 10^{18}$ α/g; Nasdala et al., 2004), in agreement with Hurley et al. (1956).

2. METHODS AND SAMPLES

2.1. Diffusion Experiments

Using methods described in Farley et al. (1999), we performed cycled, step-heating diffusion experiments on both single- and multi-grain aliquots of zircons, using projector-bulb furnaces for all but the last step, in which remaining He was extracted by laser heating. All but one experiment utilized a heating schedule beginning at low temperature (300 or 310°C), and cycling between high (500–550°C) and low T several more times (Table 1). Use of the same schedule in these experiments, with minor (<10%) variations in the timestep durations, allows straightforward comparisons of Arrhenius and $\ln(a/a_0)$ plots for different samples. This standard heating schedule did not include multiple isothermal steps at the beginning of the experiment, to avoid obscuring deviations from simple Arrhenius behavior at low fractions of cumulative degassing. One diffusion experiment did utilize multiple isothermal steps at relatively low temperatures (325°C and 425°C) in the initial stages of degassing, to explore the dependence of Arrhenius and $\ln(a/a_0)$ trends on heating schedule.

Three experiments used whole zircons from the Cretaceous Cornucopia stock of the southern Wallowa Mountains, Oregon. These zircons were selected because their age, U-Th contents, size, and other characteristics are typical of commonly dated zircons in many thermochronometric studies. In addition, aside from the effects of α-ejection, intracrystalline He distribution is likely relatively homogeneous, because electron microprobe imaging shows that U-Th zonation is not strong, there are relatively few inclusions in the crystals, and as described below, their host rocks cooled relatively rapidly.

There is some debate about the precise emplacement age of the Cornucopia stock. Early K/Ar dates range from 118–136 Ma (Armstrong et al., 1977), but Johnson et al. (1997) favored an intrusion age of 116.8 ± 2.4 Ma (2σ), based on biotite $^{40}Ar/^{39}Ar$ dating. However, our unpublished data from a related study of thermochronologic effects of dike-heating in this area yield zircon U/Pb ages of 122 Ma and biotite $^{40}Ar/^{39}Ar$ ages of 120 Ma, from rocks far removed from dikes. Other data from this related study also constrain intermediate- through low-temperature thermal history of these samples. Zircon fission-track ages of ~120 Ma, and zircon and apatite (U-Th)/He and apatite fission-track ages of ~100–110 Ma, indicate that these rocks cooled relatively rapidly to temperatures less than ~70°C by the mid-Cretaceous. Zircons selected for diffusion experiments were size sorted: 01CS15Z-40 contained 19 grains with an average half-width of the tetragonal prisms (here called effective radius) of 40 μm, 01CS15Z-56 contained 11 grains at 56 μm, and 01CS15Z-66 contained 10 grains at 66 μm. One standard deviation of crystal radii in each of these aliquots was between 4 and 7 μm.

Arrhenius plots derived from step-heating experiments on typical zircons may be complicated by effects of He zonation, which can be caused by diffusive He loss, U or Th zonation, or α-ejection. To mitigate against these effects, we also performed diffusion experiments on single-grain fragments, 200, 75, and 83 μm in minimum dimension, from a much larger (1–3 cm), gem-quality zircon crystal from Sri Lanka with a U/Pb age of 567 ± 4 Ma (Nasdala et al., 2004). Previous work has shown that these crystal have unit-cell dimensions typical of weakly radiation-damaged zircon (less than would be expected for their α dosage, were not artificially heat treated, and have very uniform U and Th distributions (923 ± 17 ppm, and 411 ± 9 ppm, respectively). Two of these samples were also dated by standard procedures following the diffusion experiments. Their ages of 457 ± 21 Ma and 450 ± 20 Ma are in good agreement with ages determined on other fragments of the same grain (434 ± 20 and 433 ± 20 Ma), as well as the mean of He ages from other Sri Lankan zircons of the same suite (442 ± 9 Ma) (Nasdala et al., 2004).

2.2. Age Determinations

Most zircon (U-Th)/He ages were measured on single grains, and performed by Nd:YAG laser heating for He extraction and sector inductively coupled plasma mass spectrometry (ICP-MS) for U-Th determinations at Yale University. A few samples (see Appendix B) were measured by furnace heating and quadrupole ICP-MS. He was measured by ^{3}He isotope dilution using a quadrupole mass spectrometer following cryogenic purification. Uranium and Th were measured by ^{229}Th and ^{233}U isotope dilution using a Finnigan Element2 inductively coupled plasma mass spectrometer. α-ejection was corrected using the zircon method described in Farley (2002). Estimated 2σ uncertainty is 8% for zircon and titanite He ages, and 6% for apatite He ages. For detailed analytical procedures see Appendix B.

Samples from Alaska and the Hohonu Range, New Zealand, were analyzed by the $^{40}Ar/^{39}Ar$ method at the University of Nevada, Las Vegas, using standard procedures (see Appendix B), involving furnace step heating, and Ar isotopic measurements using a MAP 215–50 mass spectrometer. Samples from Stewart Island, New Zealand, were analyzed by the $^{40}Ar/^{39}Ar$ method at New Mexico Tech. K-feldspar multidomain thermal modeling followed standard procedures as outlined in Lovera et al. (1989, 1991). Conformity of models to the assumptions of the technique was assessed by a correlation coefficient (C_{fg}) between age and $\log(r/r_0)$ spectra (Lovera et al., 2002). All $^{40}Ar/^{39}Ar$ analytical data are reported at the confidence level of 1σ (standard deviation). In figures, cooling models are shown for 90% confidence intervals of the mean (inner, gray lines) and overall distribution (outer, black lines) of multiple cooling history models. If another single model is run, there is a 90% chance it will fall within the outer lines, whereas if another set of models are run there is a 90% chance that their mean will fall within the inner lines.

2.3. Samples for Thermochronologic Intercalibration

Four samples from three areas were used for comparison between zircon (U-Th)/He ages and cooling models based on K-feldspar $^{40}Ar/^{39}Ar$ and other isotopic systems. The specific samples used were chosen partly because of their well-constrained thermal histories, and partly because they underwent moderate rates of cooling through temperatures between ~150–200°C (~20–60°C/myr). For detailed descriptions and regional geologic context of these samples, see Appendix A.

Two samples were taken from the 109 Ma Te Kinga pluton, part of the Honohu batholith west of the Alpine Fault on South Island, New Zealand (Tulloch, 1988; Waight et al., 1997). Previous work indicates that relatively rapid exhumation and cooling to temperatures of ~200°C occurred not long after crystallization of this pluton, based on a zircon U/Pb age of 108.7 ± 3.0 Ma (2σ) and muscovite-whole rock and biotite-whole rock Rb/Sr isochron ages of 104.0 ± 2.0 Ma and 73.6 ± 2.0 Ma (2σ) (Waight et al., 1997). An apatite fission track age of 5.3 ± 1.0 Ma (2σ) reported by Spanninga (1993) defines unroofing during the most recent convergent tectonism of the Alpine Fault. Together

Table 1. Results of cycled step-heating He diffusion experiments.

Step	T °C	minutes	^{4}He (ncc STP)	f_{cum}	ln (D/a^2)
01CS15z 40 μm					
1	300	126	0.556	0.0026	−23.25
2	325	120	0.377	0.0044	−22.61
3	350	82	0.483	0.0067	−21.53
4	375	104	1.025	0.0115	−20.51
5	400	60	1.012	0.0163	−19.55
6	425	94	2.864	0.0298	−18.46
7	450	67	2.724	0.0427	−17.71
8	475	88	5.019	0.0664	−16.92
9	500	69	6.656	0.0978	−15.97
10	520	37	5.559	0.1241	−15.20
11	505	65	4.761	0.1466	−15.70
12	495	62	2.615	0.1589	−16.11
13	485	62	1.614	0.1665	−16.52
14	475	63	0.946	0.1710	−17.03
15	460	83	0.704	0.1743	−17.57
16	440	123	0.466	0.1765	−18.36
17	385	872	0.368	0.1783	−20.54
18	380	1011	0.271	0.1795	−20.99
19	535	67	7.103	0.2131	−14.90
20	467	87	0.782	0.2168	−17.26
21	462	92	0.604	0.2196	−17.55
22	368	4009	0.507	0.2220	−21.49
23	550	60	8.570	0.2625	−14.34
Final			156.19	1	
Total			211.78		
01CS15z 56 μm					
1	300	126	0.995	0.0025	−23.39
2	325	120	0.972	0.0049	−22.27
3	350	82	1.123	0.0076	−21.21
4	375	106	2.266	0.0132	−20.25
5	400	60	2.229	0.0187	−19.27
6	425	95	5.799	0.0330	−18.29
7	450	97	8.602	0.0543	−17.36
8	475	88	10.721	0.0808	−16.59
9	500	72	12.771	0.1123	−15.83
10	520	37	8.871	0.1342	−15.26
11	505	65	7.750	0.1533	−15.79
12	495	62	5.312	0.1665	−16.00
13	485	62	3.279	0.1746	−16.41
14	475	63	1.815	0.1790	−16.97
15	460	90	1.795	0.1835	−17.31
16	440	134	0.971	0.1859	−18.30
17	385	923	0.606	0.1874	−20.69
18	380	1069	0.547	0.1887	−20.93
19	535	67	13.118	0.2211	−14.88
20	467	87	1.547	0.2249	−17.18
21	462	92	1.140	0.2277	−17.52
22	368	4009	0.925	0.2300	−21.49
23	550	61	13.967	0.2645	−14.49
Final			297.83	1	
Total			404.95		
01CS15z 66 μm					
1	300	162	0.694	0.0015	−24.56
2	325	128	0.352	0.0023	−24.09
3	350	95	0.507	0.0035	−23.02
4	375	137	1.200	0.0061	−22.02
5	400	99	1.663	0.0098	−20.86
6	425	94	4.054	0.0189	−19.33
7	450	67	4.460	0.0288	−18.39
8	475	88	9.672	0.0504	−17.35
9	500	69	10.550	0.0739	−16.55
10	520	37	8.188	0.0922	−15.87
11	505	65	6.469	0.1066	−16.48
12	495	60	3.962	0.1154	−16.77
13	485	62	2.717	0.1215	−17.11
14	475	63	3.595	0.1295	−16.78
15	460	83	1.310	0.1324	−18.02
16	440	123	0.882	0.1344	−18.79
17	385	870	0.700	0.1359	−20.96
18	380	1003	0.795	0.1377	−20.96
19	535	67	13.122	0.1670	−15.33
20	467	87	1.403	0.1701	−17.71
21	462	92	1.266	0.1729	−17.85
22	368	4009	1.124	0.1754	−21.72
23	550	60	15.201	0.2093	−14.80
Final			354.68	1	
Total			448.57		
M146 100 μm					
1	300	164	1.086	0.0016	−24.57
2	325	131	0.739	0.0026	−23.75
3	350	120	1.139	0.0042	−22.73
4	375	137	2.137	0.0073	−21.71
5	400	108	2.670	0.0111	−20.78
6	425	111	4.421	0.0174	−19.87
7	450	67	4.300	0.0235	−19.03
8	475	95	9.407	0.0370	−18.20
9	500	73	9.233	0.0501	−17.56
10	520	39	6.669	0.0597	−17.02
11	505	65	5.338	0.0673	−17.60
12	495	86	4.682	0.0740	−17.90
13	485	63	1.950	0.0768	−18.39
14	475	69	1.383	0.0787	−18.79
15	460	86	0.972	0.0801	−19.34
16	440	123	0.595	0.0810	−20.18
17	385	870	0.442	0.0816	−22.42
18	380	1014	0.422	0.0822	−22.61
19	535	67	9.276	0.0954	−16.72
20	467	90	0.956	0.0968	−19.20
21	462	87	0.725	0.0978	−19.43
22	368	3860	0.629	0.0987	−23.35
23	550	60	10.259	0.1134	−16.31
Final			621.11	1	
Total			700.54		
M146 38 μm					
1	300	164	1.117	0.0035	−22.94
2	325	129	0.536	0.0052	−22.53
3	350	96	0.744	0.0075	−21.52
4	375	140	1.468	0.0121	−20.79
5	400	110	1.951	0.0182	−19.82
6	425	94	2.066	0.0247	−19.26
7	450	67	2.439	0.0324	−18.47
8	475	91	4.687	0.0471	−17.80
9	500	68	4.869	0.0624	−17.10
10	520	37	4.058	0.0751	−16.44
11	505	67	3.594	0.0864	−16.98
12	495	64	2.017	0.0927	−17.40
13	485	62	1.212	0.0965	−17.82
14	475	72	0.954	0.0995	−18.17
15	460	85	0.610	0.1014	−18.76
16	440	148	0.503	0.1030	−19.49
17	385	873	0.321	0.1040	−21.70
18	380	1165	0.301	0.1049	−22.04
19	535	67	5.830	0.1232	−16.12
20	467	87	0.632	0.1252	−18.51
21	462	95	0.509	0.1268	−18.80
22	368	3931	0.419	0.1281	−22.70
23	550	60	5.813	0.1463	−15.81
Final			272.12	1	
Total			318.77		
M146 isothermal					
1	325	177	1.794	0.0034	−23.06
2	325	223	0.791	0.0049	−23.22
3	325	159	0.420	0.0057	−23.27
4	325	1081	1.606	0.0088	−23.54
5	325	1302	1.374	0.0114	−23.55
6	325	404	0.336	0.0121	−23.64
7	325	913	0.676	0.0133	−23.68
8	325	457	0.298	0.0139	−23.73
9	325	6774	2.717	0.0191	−24.03
10	325	1260	0.458	0.0200	−23.96
11	325	7266	1.921	0.0236	−24.17
12	325	3035	0.794	0.0251	−24.06
13	400	111	1.188	0.0274	−20.28
14	425	60	1.322	0.0300	−19.47
15	425	68	1.235	0.0323	−19.58
16	425	809	8.571	0.0486	−19.86
17	425	240	1.754	0.0520	−19.97
18	425	943	5.497	0.0625	−20.06
19	425	107	0.535	0.0635	−20.11
20	450	90	1.191	0.0658	−19.11
21	475	60	1.918	0.0694	−18.18
22	500	60	4.108	0.0772	−17.34
23	380	6694	2.560	0.0821	−22.44
24	460	60	0.807	0.0837	−18.83
25	550	60	13.657	0.1097	−15.84
Final			466.83	1	
Total			524.36		

ln(D/a^2) calculated using equations of Fechtig and Kalbitzer (1966).

these data indicate a cooling history for the Te Kinga monzogranite which is consistent with other data from the Hohonu Batholith. U/Pb, Rb/Sr, and fission-track data were reported for sample KFR7, which was collected at 120 m elevation and ~2 km from the Alpine fault. Sample TK7 was collected near the center of the pluton at 1200 m elevation and ~4 km from the Alpine Fault (see Appendix A for detailed location information on these and other samples).

The third sample is from the Southwest Arm granite, from central Stewart Island, off the southern tip of South Island, New Zealand. A U/Pb crystallization age of 167 ± 2 Ma (2σ) has been determined for this granite (Tulloch, 2003; Tulloch et al., in review), but no other geochronological constraints on this pluton exist. To better establish the cooling history we analyzed both hornblende and K-feldspar by the $^{40}Ar/^{39}Ar$ method, and obtained titanite, zircon, and apatite (U-Th)/He ages.

The fourth sample is from the Speel River pluton, part of the late Cretaceous to early Tertiary Coast Plutonic Complex in southeast Alaska. This sample was collected near sea level, in Tracy Arm of Holkham Bay, approximately 200 km south of Juneau. Gehrels et al. (1991) obtained a zircon U/Pb age of $60.4\ ^{+1.3}_{-3.0}$ Ma for the Speel River pluton. Wood et al. (1991) reported hornblende, biotite, and plagioclase $^{40}Ar/^{39}Ar$ ages of 56.9 ± 0.6 Ma, 54.1 ± 0.3 Ma, and 50.7 ± 0.9 Ma, respectively, for the same sample analyzed in this study, thus showing relatively rapid cooling through ~200°C by 50 Ma. Donelick (1986) reported an apatite fission-track age of 32.6 ± 3.6 Ma for this same sample. Apatite and zircon (U-Th)/He ages for a larger sample set, including vertical transects and other sea level samples from this and an adjacent region, were presented by Hickes et al. (2000). We focus here only on one sea-level sample: 8500-15.

3. RESULTS

3.1. Diffusion Experiments

Step-heating data and Arrhenius plots for diffusion experiments are shown in Table 1 and Figures 1 and 2. For all experiments using the standard heating schedule, different slopes and intercepts of trends can be distinguished for steps before and after heating to temperatures of ~470–495°C, similar to most of the results of Reiners et al. (2002a). In most cases, trends formed by steps subsequent to heating to these temperatures have steeper slopes, and there is little change in slope after these steps. The only standard-heating-schedule experiment that does not show this pattern is the largest size-split of 01CS15z, but this sample also shows more complex slope changes in the initial degassing steps, and one anomalously high apparent diffusivity step in a post-high-temperature heating step at 475°C. These complications may be due to relatively abundant inclusions in several of the zircons in this aliquot.

The experiment involving multiple low-temperature isothermal steps shows apparently decreasing diffuvisity in both the 325°C and 425°C steps. Apparent diffusivity at constant temperature decreases one log unit in the first 12 steps at 325°C, and one-half log unit further in the six steps at 425°C (Table 1; Fig. 1). The subsequent steps show results similar to those of the other diffusion experiments.

Activation energies (E_a) and frequency factor/diffusion dimension parameters (D_0/a^2) for these data are shown in Table 2. For the purposes of discussion, in all but the isothermal diffusion experiment we distinguish Arrhenius trends derived from step-heating cycles before ("pre-high-T"), and subsequent to ("post-high-T"), the first heating steps at high temperature (520°C). For the other experiment we refer to all steps after the 425°C isothermal steps as the "post-high-T" steps. To remove potential variations in frequency factors (D_0) due to grain-size variations (assuming that diffusion domain size is equivalent to grain size; discussed later), we multiply each D_0/a^2 by the square of the average grain radius for each experiment, to derive the frequency factor, D_0. Post-high-T steps for the five experiments with the standard heating schedule yield E_a and D_0 ranging from 163–173 kJ/mol (39–41 kcal/mol), and 0.09–1.5 cm^2/s, respectively. Both E_a and D_0 for initial steps are more variable, and consistently lower (Table 2). Post-high-T steps of the experiment with multiple low-T isothermal steps yields E_a of 174 kJ/mol (41.6 kcal/mol) and D_0 of 0.27 cm^2/s, similar to the other experiments.

Closure temperatures (T_c, Dodson, 1973; calculated assuming cooling rates of 10°C/myr) from post-high-T steps are 173–195°C, and form a much narrower range than T_c values calculated from all steps (129–173°C) or from pre-high-T steps (111–171°C) (Table 2). Assuming that the diffusion domain size (a) is equivalent to the size of the minimum dimension of the grains, then these T_c are more properly compared for a single a, which we assume here to be 60 μm. Using this method, T_c calculated from post-high-T steps are 171–196°C, T_c from all steps are 139–172°C, and those from pre-high-T steps are 123–169°C.

3.2. Thermochronologic Data

All (U-Th)/He and $^{40}Ar/^{39}Ar$ data are shown in Tables 3 and C1, respectively. Zircon He ages of individual crystals (or aliquots in the Alaskan case) are shown with 8% error bars, corresponding to two standard deviations observed on replicate single-grain Fish Canyon Tuff zircon He ages in the Yale He chronometry laboratory rather than formal analytical precision on He and U-Th measurements, which is ~2%. Actual reproducibilities observed in these samples are often considerably different (both better and worse) than this error estimate, but we prefer to use an uncertainty based on reproducibility of Fish Canyon Tuff zircon rather than each specific sample, due to the relatively small number of analyses for most of these samples. Means of zircon He ages are shown with error bars corresponding to two standard deviations of ages from each sample, except for the Holkham Bay sample, since it includes only two analyses. For this sample, we use 8% (2σ) error bars.

3.3. Te Kinga Pluton

Biotite, muscovite, and K-feldspar $^{40}Ar/^{39}Ar$ step-heating data are given in Table C1, K-feldspar models are shown in Figure 3, and all data, along with published zircon U/Pb and apatite fission-track data, are shown in Figure 4. The correlation coefficient, C_{fg}, of the K-feldspar Ar release data for sample KFR7 is 0.93 and that for sample TK7 is 0.88. This demonstrates good correspondence between measured age and log r/r_o spectra, and validates extrapolation of diffusion parameters measured in the laboratory to geologic conditions (Lovera et al., 2002). Both samples TK7 and KFR7 show cooling curves characterized by slow cooling rates at temperatures of about ~300°C beginning at ~70–80 Ma, followed by a break to more rapid cooling below 200–300°C at 15–20 Ma. Sample KFR7 shifts more abruptly to more rapid cooling below 300°C than TK7, and does so later than TK7, at ~17–18 Ma rather than 20 Ma.

Zircon (U-Th)/He ages are shown in Table 3 and Figure 4 along with confidence intervals from K-feldspar models in Figure 3. Three single-grain replicates from KFR7 have ages

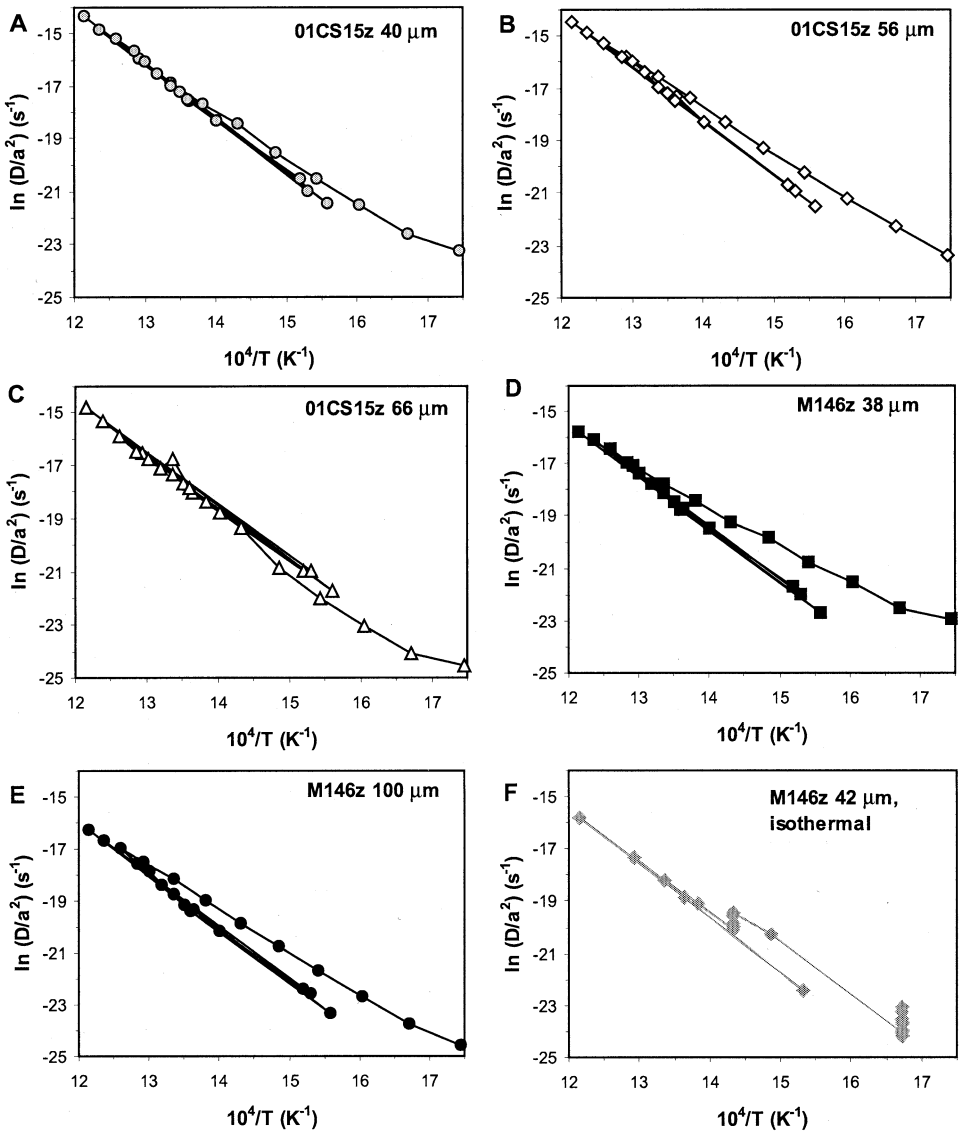

Fig. 1. Arrhenius plots of cycled step-heating He diffusion experiments on zircons. Stated accuracy of thermocouples used for temperature measurement is ± 2–3°C, which yields x-axis error bars the same size as or less than symbols. Experiments shown in A through E used the same cycled step-heating schedule; experiment F involved multiple isothermal steps at 325 and 425°C in the initial stages (see Table 1). Experiments A-E show decreasing apparent diffusivity in initial up-temperature steps, but relatively linear behavior after heating to ~450–500°C, similar to results for titanite (Reiners and Farley; 1999 and previous zircon experiments (Reiners et al., 2002a).

between 8.3 ± 0.7 and 8.5 ± 0.7 Ma. The closure temperatures calculated for these grains, based on crystal sizes and a cooling rate of 21°C/myr (from the 293–188°C range of the K-feldspar model) are 179–186°C. Although these temperatures and ages do not overlap directly with the cooling models for K-feldspar, the average zircon He age of 8.4 ± 0.1 Ma is consistent with a linear extrapolation of the K-feldspar cooling model.

Five single-grain replicates from sample TK7 have ages between 11.5 and 20.4 Ma, with an average of 15.6 ± 7.6 Ma (2σ). The reproducibility on these samples (and error on the mean) is considerably worse than the 2σ errors of 8% observed for Fish Canyon Tuff zircon He ages. For cooling rates derived from the rapid cooling part of the K-feldspar paths, and grain sizes of the dated zircon crystals, closure temperatures for these grains range from 179 to 183°C. Three out of five of these grains fall within 1σ uncertainties of the K-feldspar cooling models, but two grains are displaced to significantly older ages (18.6 ± 1.5 and 20.4 ± 1.6 Ma), although the mean of all grains still overlaps with the K-feldspar model (Fig. 4). As is the case for all samples in this study, there is no correlation between crystal size and age in these grains, as is observed for some apatites (Reiners and Farley, 2001), thus some other explanation must be sought for the older ages and relatively poor reproducibility of this sample.

3.4. Southwest Arm Pluton

Hornblende and K-feldspar $^{40}Ar/^{39}Ar$ step-heating data are given in Table C1, K-feldspar models are shown in Figure 5,

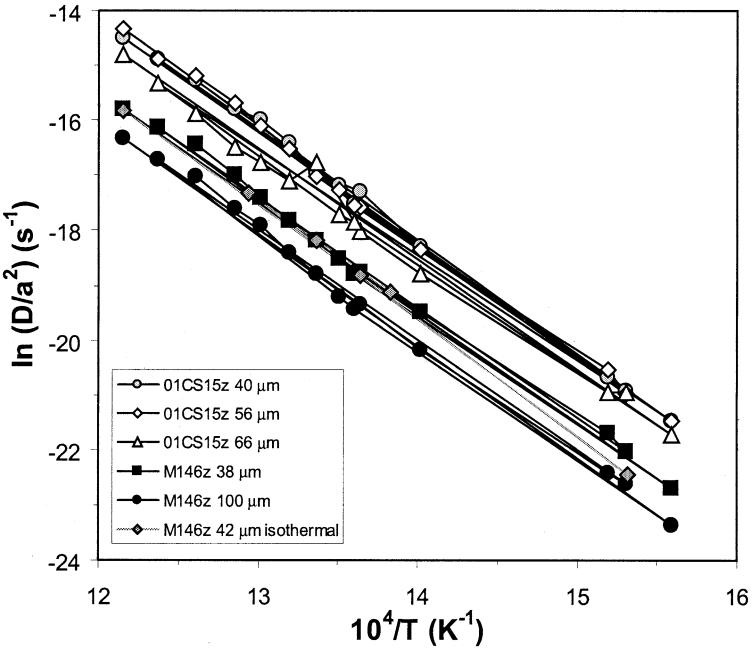

Fig. 2. Arrhenius trends for all diffusion experiments showing only steps after the post-high-*T* (defined as first step at 520°C; see text) steps for samples A–E of Figure 1, and only steps following the isothermal steps at 425°C for sample F of Figure 1.

and all data are shown, along with existing zircon U/Pb data, in Figure 6. The C_{fg} of the K-feldspar Ar release data for this sample is 0.94. The zircon and hornblende ages suggest a relatively high cooling rate in the late Jurassic through a temperature of ~500°C. The K-feldspar cooling model shows average cooling rates of ~10°C/myr from ~100–80 Ma, but there is a suggestion of a two-phase cooling history, with a concave portion of decreasing cooling rates to ~85 Ma, followed by more rapid cooling (~20°C/myr) from 85–80 Ma.

Titanite, zircon, and apatite (U-Th)/He ages are shown in Table 3 and Figure 6. Assuming a closure temperature of 200°C, titanite He ages of 92.7 ± 7.4 and 85.4 ± 6.8 Ma (2σ)

Table 2. Diffusion parameters derived from step-heating experiments.

	log (D_0/a^2)	1σ	D_0 (cm^2/s)	1σ	E_a [kJ/mol, (kcal/mol)]	1σ	T_c (°C)	1σ	T_c a = 60 μm
01CS15z 40 μm									
post-high T	4.7100	0.1615	0.8392	$+0.3781\ -0.2607$	173 (41.2)	1.1	179	6.4	196
pre-high T	2.5240	0.3301	5.47×10^{-3}	$+6.23 \times 10^{-3}\ -2.91 \times 10^{-3}$	141 (33.6)	2.1	141	13	
all steps	3.018	0.3191	0.0171	$+0.0185\ -0.0089$	148 (35.4)	2.2	151	13	
01CS15z 56 μm									
post-high T	4.6860	0.1489	1.509	$+0.6166\ -0.4379$	172 (41.1)	0.25	178	5.9	180
pre-high T	2.6250	0.1271	0.0131	$+0.0045\ -0.0033$	141 (33.7)	0.20	139	5.2	
all steps	2.9320	0.3369	0.0266	$+0.0312\ -0.0143$	147 (35.0)	0.55	148	14	
01CS15z 66 μm									
post-high T	3.8516	0.3030	0.3076	$+0.3104\ -0.1545$	163 (39.0)	0.51	173	12	171
pre-high T	3.8080	0.5446	0.1384	$+0.3467\ -0.0989$	160 (38.1)	0.85	171	22	
all steps	3.5047	0.2866	0.2784	$+0.2601\ -0.1345$	163 (38.9)	0.46	173	12	
M146 100 μm									
post-high T	3.7480	0.1734	0.5604	$+0.2750\ -0.1875$	170 (40.7)	0.29	195	7.4	185
pre-high T	1.3680	0.1690	2.33×10^{-3}	$+1.11 \times 10^{-3}\ -7.52 \times 10^{-4}$	134 (31.9)	0.26	145	7.4	
all steps	1.5520	0.4436	3.56×10^{-3}	$+6.33 \times 10^{-3}\ -2.28 \times 10^{-3}$	138 (32.9)	0.72	155	20	
M146 38 μm									
post-high T	3.8190	0.1700	0.0927	$+0.0404\ -0.0297$	168 (40.0)	0.26	186	6.5	195
pre-high T	0.2406	0.2849	2.45×10^{-5}	$+2.27 \times 10^{-5}\ -1.18 \times 10^{-5}$	114 (27.2)	0.44	111	13	
all steps	0.8270	0.5524	9.44×10^{-5}	$+2.42 \times 10^{-4}\ -6.80 \times 10^{-5}$	124 (29.6)	0.90	129	25	
M146 isothermal									
post 425°C steps	4.2186	0.2680	0.2704	$+0.2313\ -0.1247$	174 (41.6)	0.46	194	11	202

Note: 1σ uncertainties reflect those from linear regression data in Arrhenius plots only. 1σ on T_c's are determined from difference of calculated T_c and T_c assuming maximum E_a combined with minimum D_0, within 1σ uncertainties, and vice versa. See text for definitions of pre-high-*T* and post-high-*T* steps of diffusion experiments.

Table 3. (U-Th)/He data.

Sample	# grains	ng U	ng Th	raw age (Ma)	F_T	corr age (Ma)	est 2σ +/− (Ma)	radius (μm)	mass (μg)	U (ppm)	Th (ppm)	Th/U	He (nmol/g)
Southwest Arm pluton, Stewart Island, New Zealand													
Zircons													
SWAzI	1	0.61	0.50	50.9	0.663	76.8	6.1	28.8	2.07	294	241	0.818	96.7
SWAzK	1	0.39	0.37	51.1	0.614	83.3	6.7	25	1.27	306	291	0.953	104
SWAzF	1	0.82	0.51	58.9	0.673	87.5	7.0	30.3	2.14	384	239	0.622	141
SWAzL	1	0.33	0.29	54.1	0.617	87.6	7.0	25	1.32	253	218	0.860	89.1
SWAZC	1	1.12	0.66	54.3	0.708	76.8	6.1	36.5	2.82	397	232	0.586	133
SWAzH	1	0.25	0.21	49.6	0.617	80.5	6.4	26.3	1.19	207	180	0.871	67.0
SWAzJ	1	1.24	1.03	58.9	0.678	86.9	7.0	31.3	2.25	553	456	0.824	211
SWAzN	1	0.77	0.66	54.9	0.638	86.1	6.9	28	1.46	531	453	0.854	189
SWAZb	2	1.57	0.78	53.3	0.631	84.4	6.8	27.1	3.28	480	237	0.494	154
SWAZHa	2	2.29	1.55	52.6	0.649	81.0	6.5	27.5	3.55	646	438	0.677	213
average						83.1							
1 stdev						4.16							
Apatites													
SWAapC	7	0.40	2.08	36.5	0.667	54.8	3.3	41.2	24.4	16.6	85.2	5.138	7.26
SWAapE	11	0.35	1.85	36.7	0.674	54.5	3.3	42	22.6	15.4	81.8	5.315	6.90
SWAapA	7	0.28	1.89	45.0	0.746	60.4	3.6	57.1	29.8	9.54	63.5	6.655	5.98
Titanites													
SWAtitA	1	0.71	5.79	92.7	1.000	92.7	7.4	nd	nd	nd	nd	nd	nd
SWAtitC	1	2.09	12.21	85.4	1.000	85.4	6.8	nd	nd	nd	nd	nd	nd
Te Kinga pluton, sample TK7													
TK7zA	1	6.80	0.86	11.6	0.778	15.0	1.2	41.8	9.72	700	88.9	0.127	45.1
TK7zB	1	0.641	0.41	15.6	0.762	20.4	1.6	41	6.84	93.7	59.6	0.636	203
TK7zC	1	2.77	0.95	9.25	0.807	11.5	0.9	49	15.3	181	62.1	0.343	9.74
TK7zD	1	3.54	0.46	14.5	0.776	18.6	1.5	43.3	7.92	447	58.5	0.131	804
TK7zE	1	10.77	1.44	10.4	0.815	12.8	1.0	52.8	14.8	730	97.3	0.133	42.3
average						15.7							
1 stdev						3.81							
Te Kinga pluton, sample KFR7													
KFR7zA	1	13.41	1.09	7.07	0.830	8.52	0.68	58.8	18.5	726	58.8	0.081	28.2
KFR7ZD	1	2.84	0.27	6.51	0.767	8.49	0.68	42.0	6.62	430	40.0	0.093	15.4
KFRzE	1	2.61	0.15	6.21	0.745[a]	8.34	0.67	48.3	4.83	539	31.3	0.058	18.3
BUKFR7zH	1	2.19	0.29	5.54	0.669	8.28	0.66	35.5	4.65	471	63.2	0.13	14.5
average						8.41							
1 stdev						0.12							
Coast Plutonic complex, sample 8500-15, sea level at Holkham Bay													
850015Z	2	2.96	0.69	37.1	0.749	49.52	4.0	36.3	8.52	347	80.7	0.232	73.3
850015Z2	2	3.66	1.20	38.3	0.781	49.08	3.9	43.7	12.3	298	97.9	0.329	66.5
average						49.3							
1 stdev						0.32							
Apatites													
850015A1	8	3.36	1.81	6.09	0.788	7.73	0.46	61.4	61.4	54.7	29.5	0.540	2.02
850015A2	11	3.71	2.09	5.97	0.775	7.71	0.46	57.3	72.8	50.9	28.6	0.563	1.85
850015A2b		2.42	1.24	6.40	0.790	8.10	0.49		44.2	54.8	28.2	0.514	2.12
850015A3	8	1.88	1.12	5.76	0.772	7.46	0.45	50.6	38.5	48.9	29.0	0.592	1.73
850015AC	1	0.144	0.057	4.73	0.705	6.71	0.40	42.3	2.77	52.1	20.5	0.392	1.45
850015AD	1	0.138	0.084	4.82	0.670	7.24	0.44	47.8	1.95	70.5	43.0	0.610	2.11
850015AE	1	0.322	0.186	5.62	0.769	7.31	0.44	56.5	5.55	58.0	33.5	0.577	2.00
850015AF	1	0.395	0.153	5.77	0.757	7.62	0.46	51.5	5.58	70.3	27.4	0.387	2.40
average						7.49							
1 stdev						0.41							

[a] F_T value for zircon BUKFR7zH has been multiplied by 0.913, to correct for U zonation (see text). Radius is defined as average of perpendicular half-widths of tetragonal prism.

are slightly older than, but overlap within 2σ, the K-feldspar cooling models. Apatite He ages of 55–60 Ma suggest slow cooling through temperatures of ~70°C (using an approximate closure temperature based on Farley, 2000). These ages are similar to 55.8 ± 3.3 Ma apatite He ages that we measured on the nearby Escarpment pluton on Stewart Island (data not presented here).

Ten single-grain zircon He ages from the Southwest Arm pluton range from 76.8 ± 6.1 to 86.9 ± 7.0 Ma, and show an overall mean of 83.1 ± 8.3 Ma (2σ). Closure temperatures for these crystals range from 168 to 176°C, using each crystal radius and a cooling rate of 18°C/myr (from the K-feldspar cooling curve for 225–150°C). Because these zircons are small (25–37 μm in tetragonal prism half-width) relative to typically dated crystals, relatively large α-ejection corrections of 0.61–0.71 may contribute to the age scatter that is greater than the

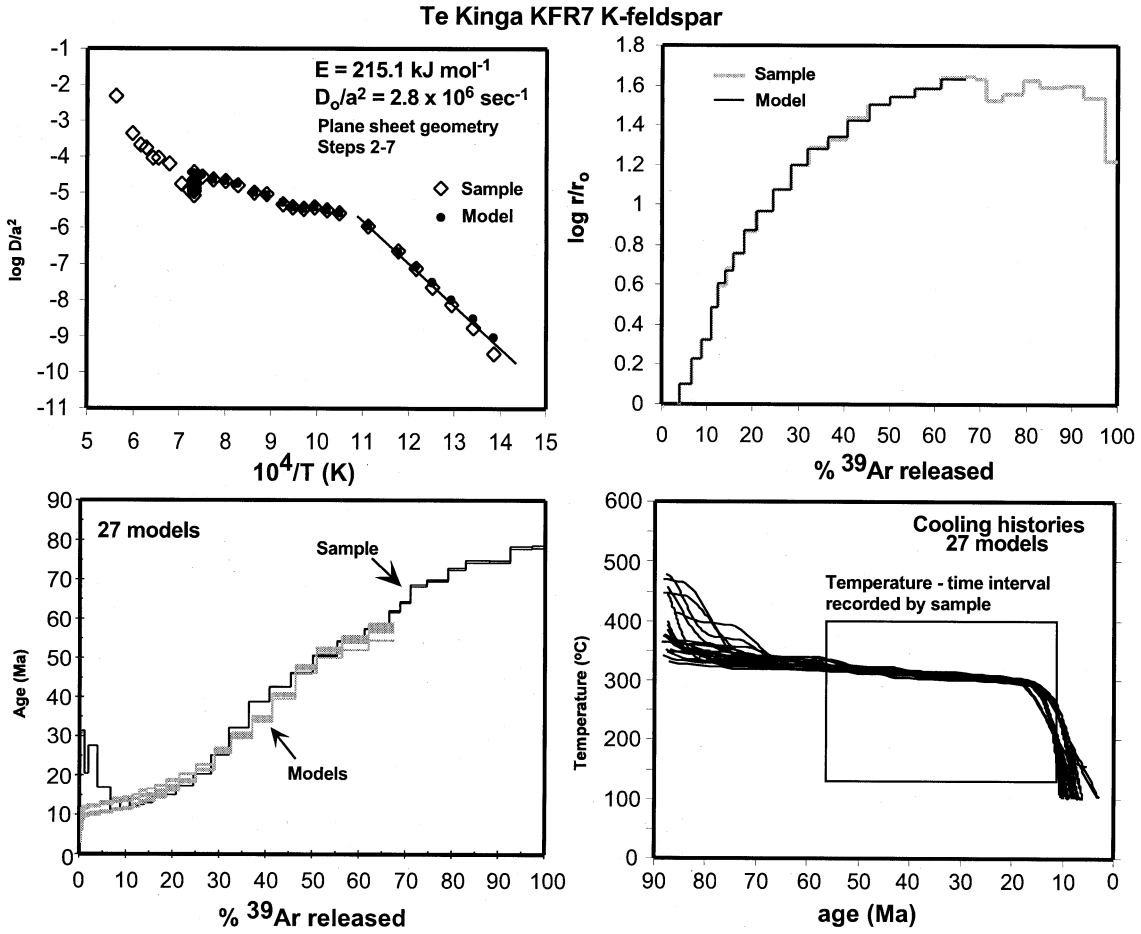

Fig. 3a. K-feldspar $^{40}Ar/^{39}Ar$ spectra and multidomain diffusion models for sample KFR7 from the Hohonu Batholith, New Zealand. (top left) Sample and model Arrhenius plots. E and D_o/a^2 are derived from linear fits to indicated low-temperature steps; E and D_o are assumed to apply to all diffusion domains. (top right) Log (r/r_o) plots showing correspondence between sample and model data. (lower left) Sample age spectra with model age spectra. (lower right) Cooling histories producing model age spectra shown in C.

typically cited 8% (2σ). Nonetheless, the mean of zircon He ages (83.1 ± 8.3 Ma; 2σ) falls directly on the K-feldspar cooling curve at the mean closure temperature (171 ± 5°C; 2σ).

3.5. Tracy Arm/Holkham Bay

K-feldspar $^{40}Ar/^{39}Ar$ step-heating data and apatite and zircon (U-Th)/He data are shown in Table C1 and Figure 7, and along with all other geochronologic information on this sample in Figure 8. Taken together these data suggest a remarkably smooth hyperbolic cooling history for this sample since crystallization at 60 Ma, with a strong deceleration of cooling between ~45–55 Ma, and final cooling through ~70°C at ~7–8 Ma. The C_{fg} of the K-feldspar Ar release data for this sample is 0.92. The K-feldspar model suggests a slightly convex-up but nearly linear cooling history between ~350–160°C, from 54 to 50 Ma.

Zircon He ages were measured on aliquots of two zircons each, but crystal sizes in each aliquot were nearly identical, so uncertainty due to different size effects in α-ejection corrections is negligible. The two aliquots yielded ages of 49.5 ± 4.0 and 49.1 ± 3.9 Ma, with a mean of 49.3 ± 3.9 Ma (8% 2σ uncertainty is used on this mean, because of the small number of available analyses). The closure temperatures for these grain-aliquots are 187 and 191°C, for measured grain sizes and a cooling rate of 61°C/myr, as measured from the 220–175°C portions of the K-feldspar cooling model. Both aliquot ages fall well within uncertainty of the K-feldspar model at these temperatures.

4. DISCUSSION

4.1. Diffusion Experiments

Arrhenius plots for these data are similar to previous results for zircon (Reiners et al., 2002a), and are similar in form to those for titanite (Reiners and Farley, 1999). Using only the post-high-T heating steps (after initial 520°C step), the calculated diffusion parameters for the standard-heating-schedule experiments are fairly consistent: activation energy, E_a = 163–172 kJ/mol (39–41 kcal/mol); frequency

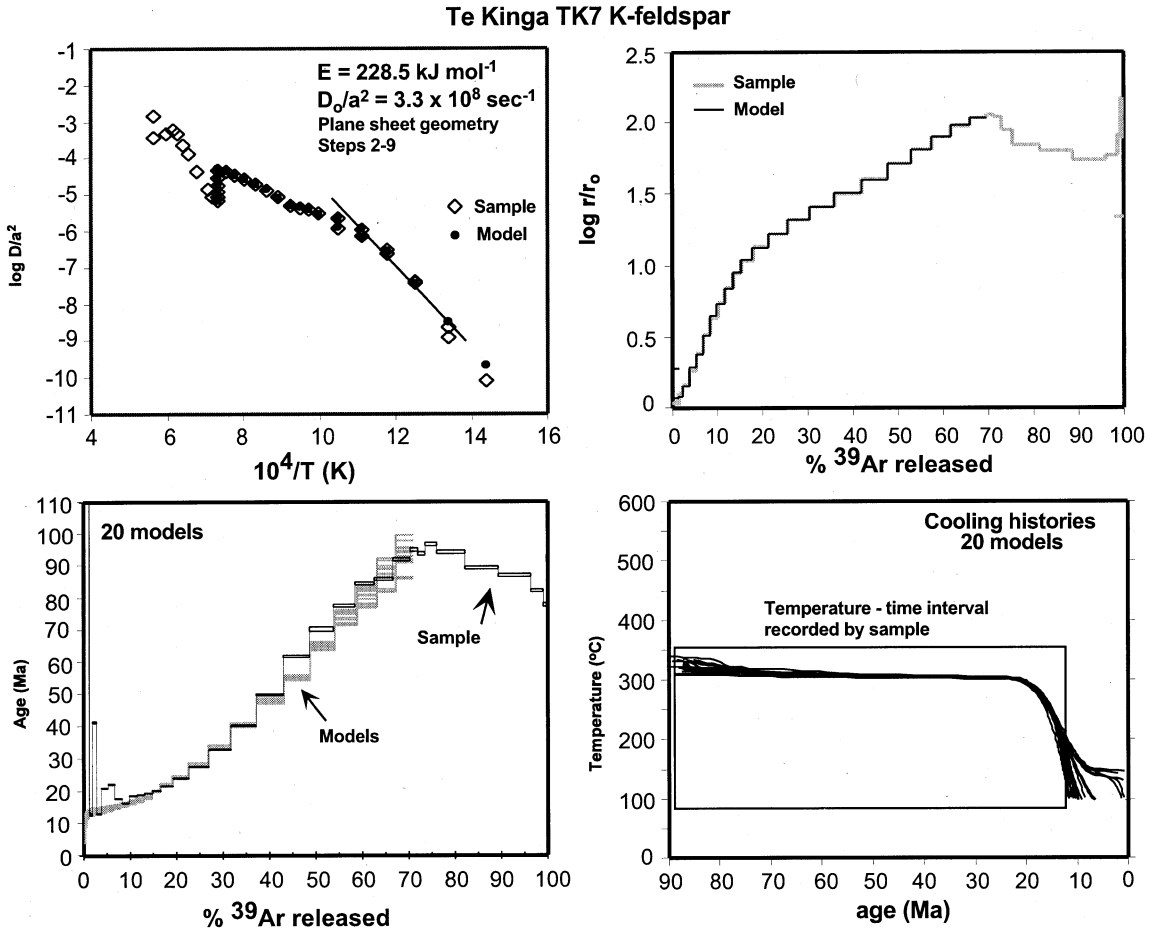

Fig. 3b. K-feldspar $^{40}Ar/^{39}Ar$ spectra and multidomain diffusion models for sample TK7 from the Hohonu Batholith. Details as in Figure 3a.

factor, D_0 = 0.09–1.5 cm^2/s. Closure temperatures, T_c for the typically cited 10°C/myr cooling rates are 173–195°C. For the experiment with low-T isothermal steps, E_a = 174 kJ/mol (41.6 kcal/mol), D_0 = 0.27 cm^2/s, and T_c = 196°C.

With the exception of the largest grain-size aliquot of 01CS15z, which shows somewhat anomalous characteristics, the larger grain-size aliquots in both the Cornucopia/Wallowa and the Sri Lankan zircons have lower D_0/a^2. Although we do not yet have enough data to confidently conclude this, it suggests that in zircon, as in titanite and apatite (Reiners and Farley, 1999; Farley, 2000), the diffusion domain size scales with the grain-size. This would suggest that closure temperatures derived from these experiments could be normalized to a common diffusion domain size, a. Correcting closure temperatures to an a = 60 μm for the standard-heating schedule experiments yields T_c of 171–196°C. The domain-size-normalized T_c for the experiment with low-T isothermal steps is slightly higher, at 202°C, but significantly fewer post-high-T steps in this experiment T_c suggest that this may be partly due to poorer precision on the parameters derived from regression of post-high-T data.

Correspondence (or at least scaling) of diffusion domain and crystal size in zircon is also supported by recent results from detrital Sri Lankan zircons (Nasdala et al., 2004). These zircons are extremely large (2–4 cm radius), and yield (U-Th)/He ages (442 ± 21 Ma) similar to those from biotite Rb-Sr (~465 Ma) in inferred basement source rocks. Zircon fission-track ages from other samples that may be derived from the same source(s) (Garver, 2002) yield much younger ages of ~45 Ma. (U-Th)/He ages similar to biotite Rb-Sr, but older than zircon fission-track ages, would imply a closure temperature above ~225–240°C, but less than ~350–450°C. If these large crystals had diffusion domain sizes of 1–2 cm, roughly half of the tetragaonal prism width of the crystals, then using the diffusion parameters from above and a cooling rate of 10°C/myr, the closure temperatures would be 305–327°C, in agreement with these constraints.

4.2. Non-Arrhenius Behavior

The apparently distinct trends of diffusivity corresponding to steps before and after the initial heating at ~475°C (Fig. 1), are inconsistent with straightforward predictions of thermally activated volume diffusion from a single domain. On the basis of simple multidomain models, Reiners and Farley (1999) suggested that this behavior in titanite could be explained by minor variations in grain size or morphology, or possibly the presence of microcracks, which would have the effect of minor diffusion

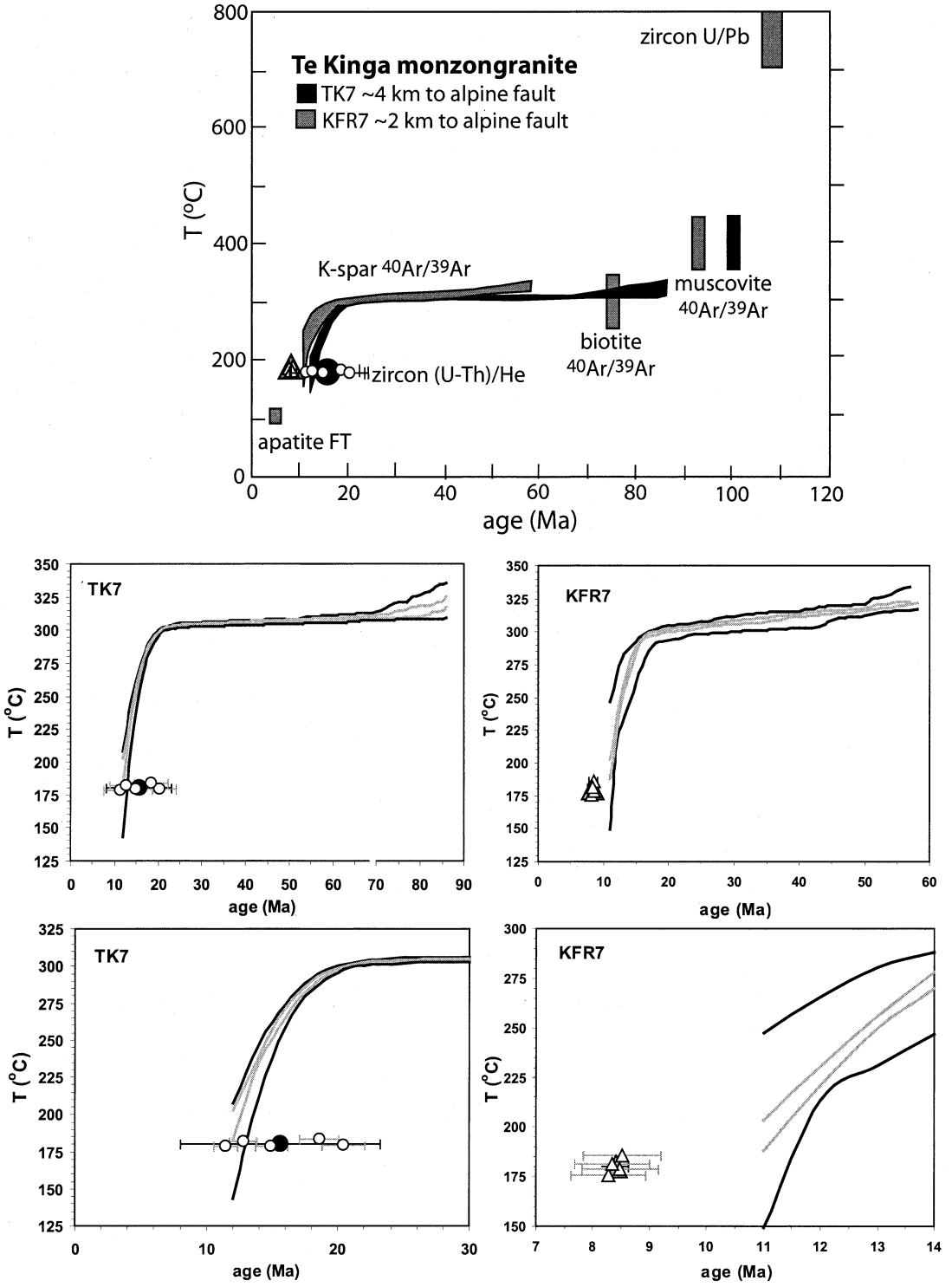

Fig. 4. Thermal histories of Te Kinga pluton samples KFR7 and TK7. Upper panel: all available data. White triangles and circles are single-grain zircon He ages. Gray and black triangles and circles are means of single-grain ages on each sample. Lower panels: Comparisons between K-feldspar $^{40}Ar/^{39}Ar$ cooling models and zircon He ages. White symbols are single-grain ages; black and gray symbols are means. Error bars on single-grain ages are 8% (2σ) estimates of reproducibility based on multiple analyses of Fish Canyon Tuff zircon. Error bars on mean ages are two standard deviations of the single-grain ages.

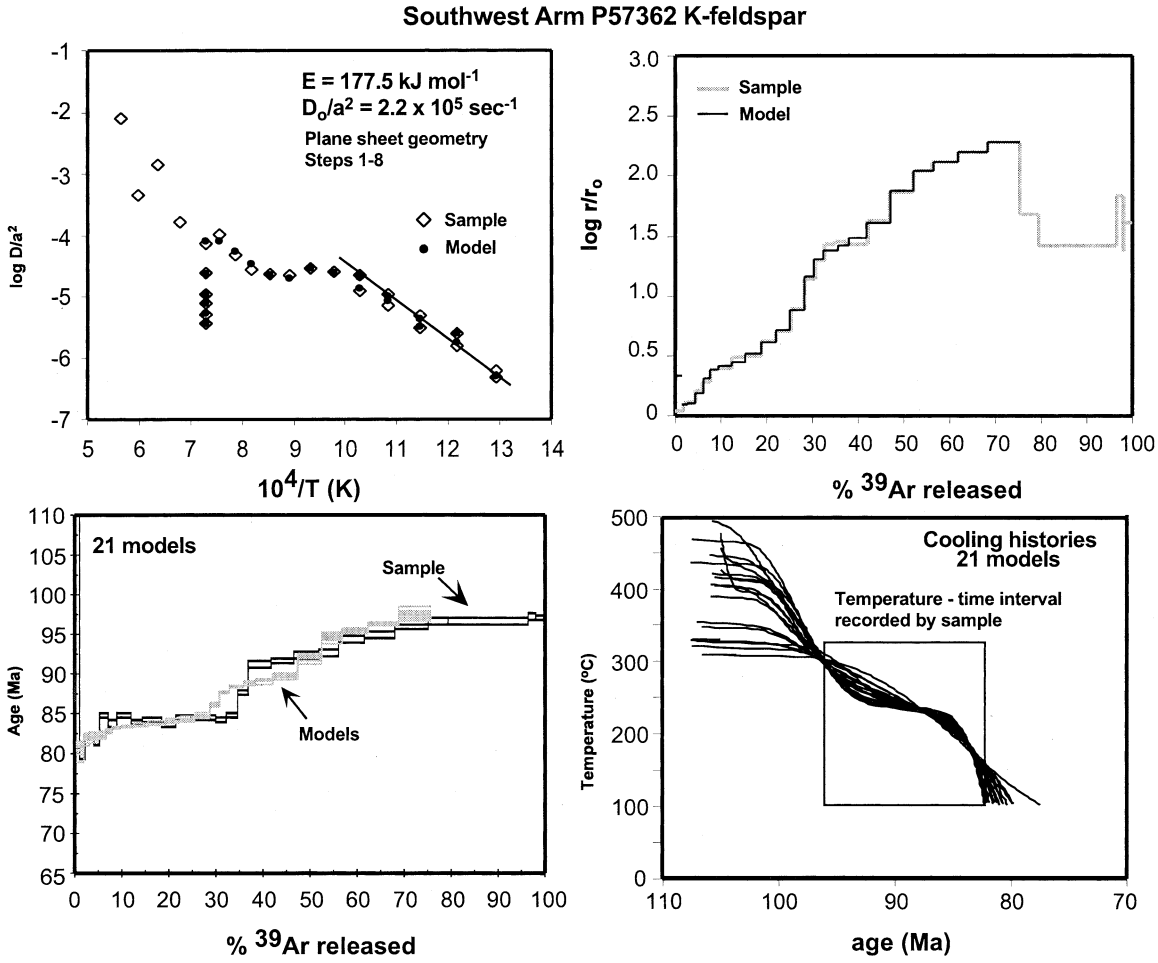

Fig. 5. K-spar $^{40}Ar/^{39}Ar$ data and multidomain diffusion models for sample from Southwest Arm pluton, Stewart Island, New Zealand. (top left) Sample and model Arrhenius plots. E and D_0/a^2 are derived from linear fits to indicated low-temperature steps; E and D_0 are assumed to apply to all diffusion domains. (top right) Log r/r_o plots showing correspondence between sample and model data. (lower left) Sample age spectra with model age spectra. (lower right) Cooling histories producing model age spectra shown in C.

domains of much smaller lengthscale than the bulk grain(s). Similar effects were also observed for apatite, and careful polishing experiments supported the hypothesis that they represent degassing of effective small domains caused by surface roughness (Farley, 2000). Here we revisit this and other potential explanations for these apparently common observations of deviations from simple Arrhenius trends. We also note that early, anomalously high diffusivity appears to be present in He diffusion experiments on not only zircon, apatite, and titanite, but also monazite, and xenotime (Farley and Stockli, 2002). In some cases, however, it is difficult to resolve this from reported data because the heating schedules used multiple low-temperature isothermal steps at the beginnings of the experiments to drive apparent diffusivity down to a trend followed by later steps. Presentation of actual He release data and heating schedules would help distinguish if this is a feature common for phases besides zircon and titanite.

Before discussing possible origins of the non-Arrhenius behavior, we note that a variation on a method of plotting step-heating diffusion data introduced by Richter et al. (1991) and Lovera et al. (1991) can be useful in assessing potential origins of this behavior. We aim to quantify the extent of deviation of apparent diffusivity (D/a^2) of early degassing steps from that of later steps, which follow a single Arrhenius trend much more closely (Figs. 1, 2). This can be expressed as:

$$\ln[(D/a^2)_{obs}/(D/a^2)_0)]$$

where $(D/a^2)_0$ is the diffusivity predicted from the Arrhenius relationship between D_0/a^2 and E_a derived from only the post-high-T steps that approximate a single linear trend, and the temperature of interest. If D of early and later steps are assumed to be equal, as in Ar diffusion from K-feldspar, then dividing this by 2 yields $\ln[a/a_0]$, similar to the $\log(r/r_0)$ of Richter et al. (1991) and Lovera et al. (1991), except our reference line (and therefore reference domain size in such an interpretation) is that of the later steps, instead of the early steps. As shown later, this expression has significance for interpretations in the context of multidomain diffusion.

Plotting $\ln(a/a_0)$ vs. cumulative fraction of He released during the experiment (Fig. 9) shows that significant deviation from a single linear Arrhenius trend is largely absent

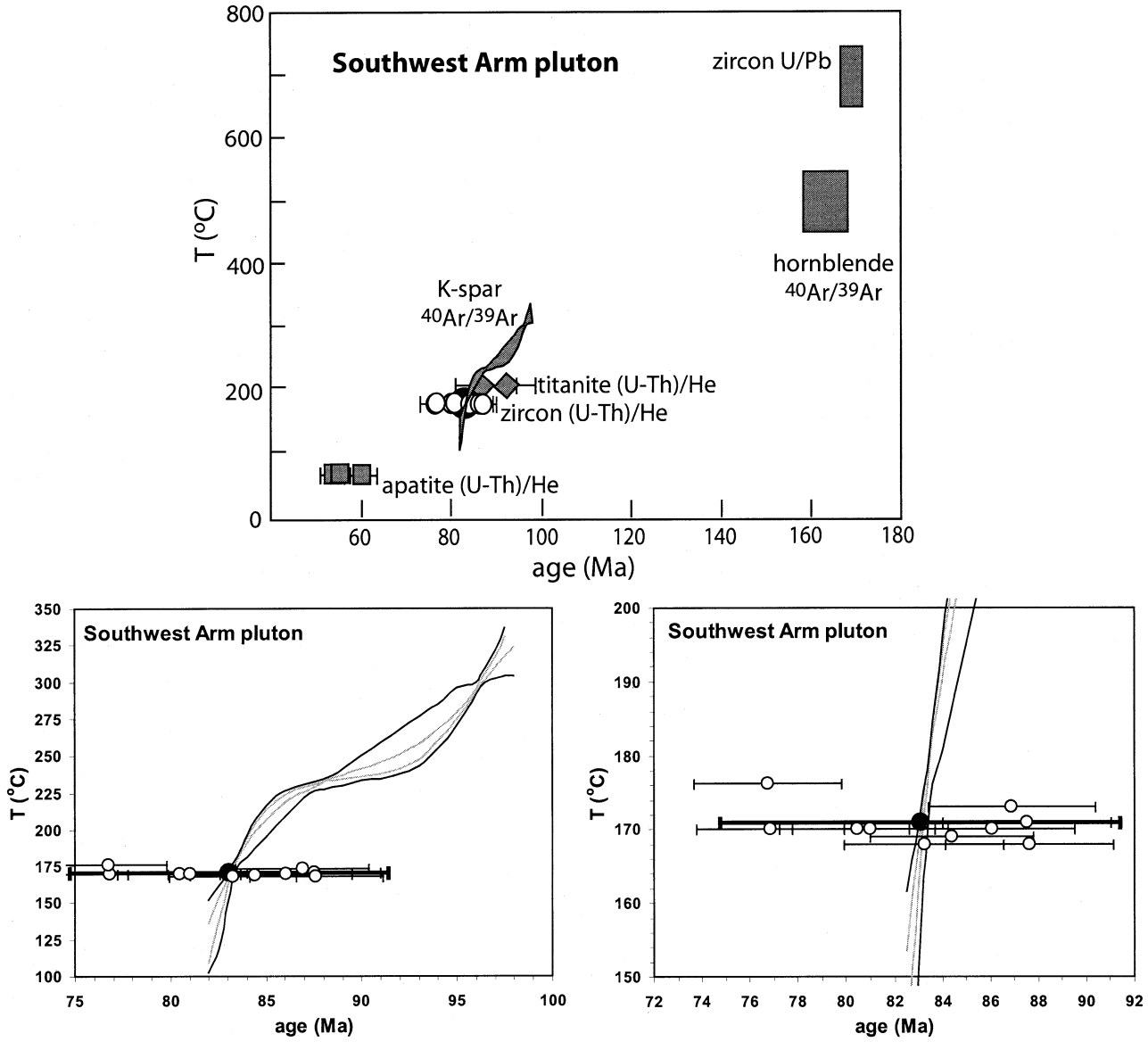

Fig. 6. Thermal histories of Southwest Arm pluton. Upper panel: all available data. Lower panels: Comparisons between K-feldspar $^{40}Ar/^{39}Ar$ cooling models and zircon He ages. White circles are single-grain ages; black circles are means. Error bars as in Figure 4.

after release of ~5–10% of gas. This also holds for the experiment involving multiple low-T isothermal steps, which suggests that this phenomenon is not related to changes in zircon properties during heating at temperatures higher than 325°C, but is simply a function of fraction of degassing. It is also noteworthy, for the modeling that follows, that for the grain sizes and heating schedules used here, the cumulative fraction of He released (f) from these samples during all heating steps is between 0.11 and 0.27. Both the relationship between $\ln(a/a_0)$ and f, as well as the absolute values of f for these heating schedules, constrain potential origins of the non-Arrhenius behavior.

Several potential origins for the initial high diffusivity and lower activation energy trends can be envisioned: 1) heterogeneous distribution of He near rapidly-diffusing sites—presumably near crystal surfaces if the diffusion domain is the grain itself; 2) progressive annealing of radiation damage during laboratory heating; 3) degassing of distinct intracrystalline domains with smaller sizes or higher diffusivity; or 4) crystallographically anisotropic diffusion. Here we investigate the plausibility of these potential origins, although we do not discuss the last one (anisotropic diffusion) beyond speculating that its results may be qualitatively similar to those predicted by a multidomain model.

4.2.1. U-Th Zoning

Helium may be heterogeneously distributed in zircons by several mechanisms. It may be depleted near crystal rims by: 1) low U-Th concentrations there, 2) diffusive loss of He during

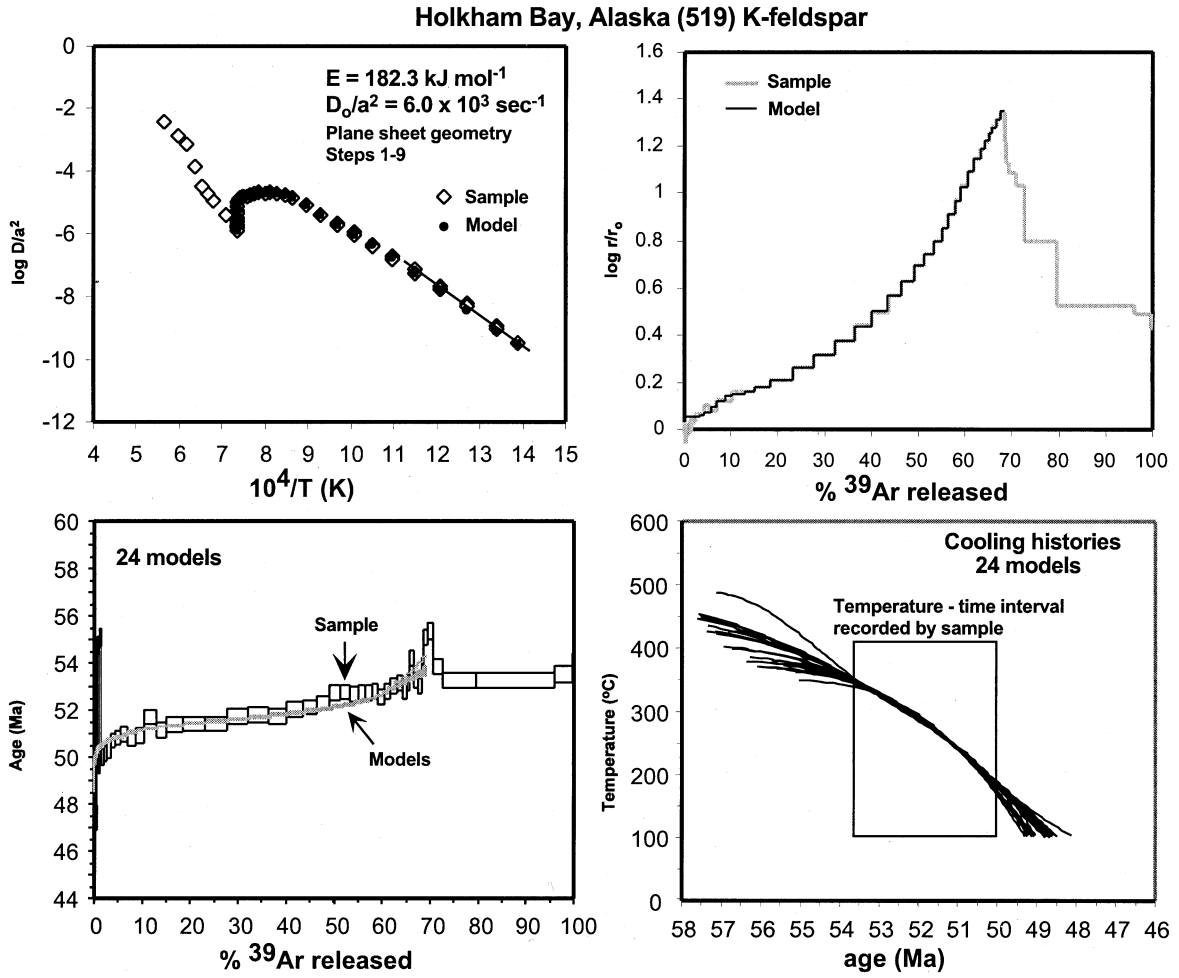

Fig. 7. K-spar $^{40}Ar/^{39}Ar$ data and multidomain diffusion models for sample 519 from Tracy Arm/Holkham Bay, Southeast Alaska. (top left) Sample and model Arrhenius plots. E and D_0/a^2 are derived from linear fits to indicated low-temperature steps; E and D_0 are assumed to apply to all diffusion domains. (top right) Log r/r_o plots showing correspondence between sample and model data. (lower left) Sample age spectra with model age spectra. (lower right) Cooling histories producing model age spectra shown in C.

protracted cooling, or 3) (α-ejection, which would affect the outer ~20 μm. Other potential complications aside, all of these scenarios would result in anomalously low apparent diffusivity in the initial steps of the experiment, disappearing in later steps. A grain-rim He-depletion effect was clearly observed for varying grain sizes of titanite (Reiners and Farley, 1999). However, the initial stages of most zircon experiments, including those in Reiners et al. (2002a) exhibit anomalously high, not low, diffusivity (a possible exception is 01CS15z-66μm; Fig. 1). If this is the result of heterogeneous He distribution, it would require systematically high He contents near the rims, presumably caused by high U and Th concentrations there. Back-scattered electron and cathodoluminesence imaging, as well as depth-profiling by laser-ablation ICP-MS, of zircons from Cornucopia-Wallowas show that roughly 30% of crystals do indeed have approximately 1.5–2 times more U-Th in a ~1–3 μm rim, usually in the pyramidal tips of the crystals. However, it is highly unlikely that this could be the explanation for the observed diffusivity changes, because all zircons, including those in the previous study (Reiners et al., 2002a) show similar behavior, which would require identical zonation. More importantly, the Sri Lankan zircons are quite homogeneous with respect to U and Th concentrations (less than 2% variation based on ion probe measurements), and interior fragments of these grains still show these apparent diffusivity changes.

4.2.2. *Radiation damage*

Radiation damage was suggested by Reiners et al. (2002a) as a possible origin for non-Arrhenius behavior of He diffusion in step-heating experiments. In this explanation, decreasing apparent diffusivity during step-heating would be due to progressive restoration of crystallinity to amorphous or lattice-damaged zones in the course of each experiment. Small increases in Raman band intensities, consistent with the onset of annealing of at least one manifestation of radiation damage, begins to occur over 1-h timescales at temperatures as low as 425°C (Zhang et al., 2000). Progressive annealing during He diffusion experiments was suggested partly on the basis of contrasting Arrhenius plots for two samples from Gold Butte with distinct

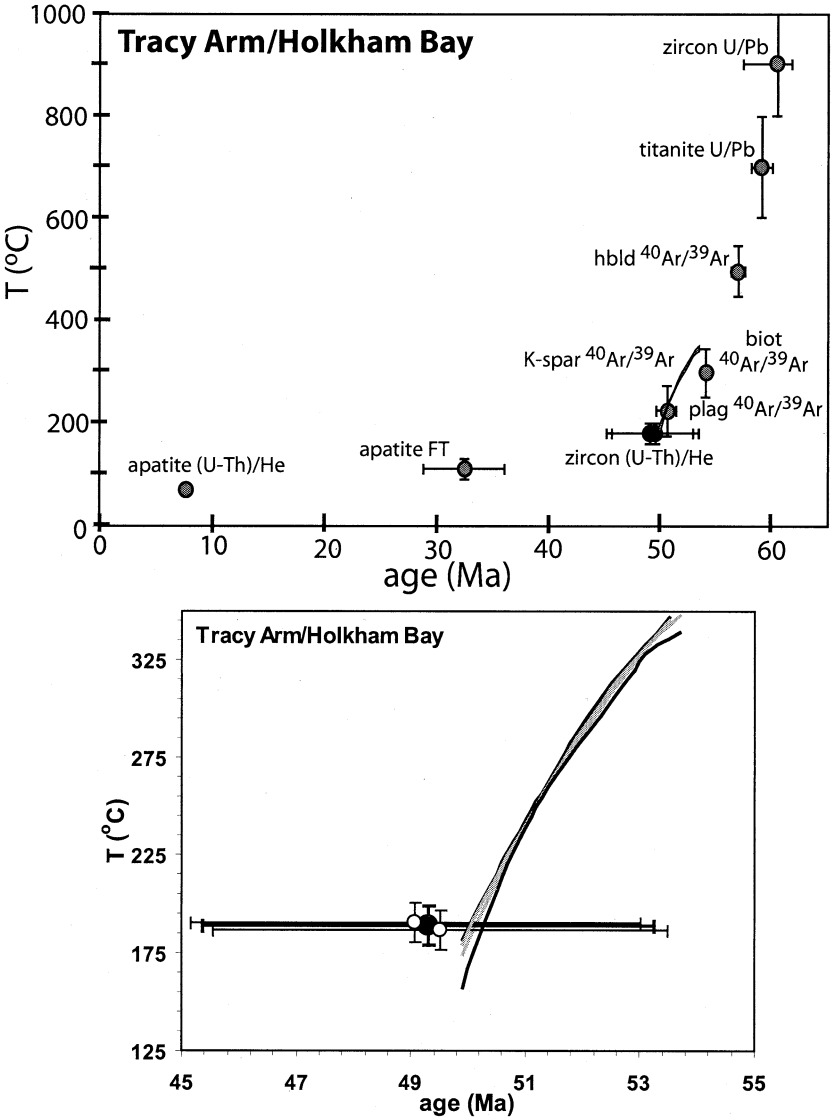

Fig. 8. Thermal histories of Coast Plutonic complex at sea level in Tracy Arm, Holkham Bay, southeast Alaska. Upper panel: all available data. Lower panels: Comparisons between K-feldspar $^{40}Ar/^{39}Ar$ cooling models and zircon He ages. White circles are single-grain ages; black circles are means. Error bars as in Figure 4, except error bars on mean are 8% (2σ).

thermal histories. Zircons with a protracted low-T thermal history showed much more erratic He release than those that had been at higher temperatures (>350°C) until relatively recently. Closer inspection of these samples, however, raises doubts about this comparison, because zircons from the sample with erratic He release contain abundant inclusions and irregular zonation patterns, whereas zircons from the other sample are remarkably homogeneous and generally inclusion-free. In addition, the diffusion experiments with multiple isothermal steps at temperatures <425°C show the same $\ln(a/a_0)$ vs. f trends as those in which temperatures range as high as 550°C, suggesting that the early non-Arrhenius behavior is a characteristic of the early-released gas, not a result of changes in zircon properties during the experiment (Figs. 1, 9).

Another reason to question the importance of radiation damage annealing during experiments on He diffusion characteristics is simply the large range of accumulated dosages and thermal histories experienced by the samples in this study, as well as those in Reiners et al. (2002a). Despite very different U-Th concentrations, ages, and thermal histories, all samples except one from Gold Butte show similar Arrhenius trends. More importantly, the Cornucopia/Wallowa and Sri Lanka zircons examined in this study also show very similar diffusion characteristics from all portions of the experiments, not just after heating at high temperature, despite the fact that their radiation dosages differ by almost two orders of magnitude. Calculated from either U/Pb or (U-Th)/He age, the Sri Lankan zircons used in this study have dosages of 1.5–2.0 $\times$ 10^{18} α/g, whereas the maximum dosage for the Cornucopia/Wallowa zircons is only ~4 $\times$ 10^{16} α/g. As shown by zircon (U-Th)/He ages reported in Nasdala et al. (2004), radiation dosages of at least 2.5–3.0 $\times$ 10^{18} α/g, and retention of this damage by

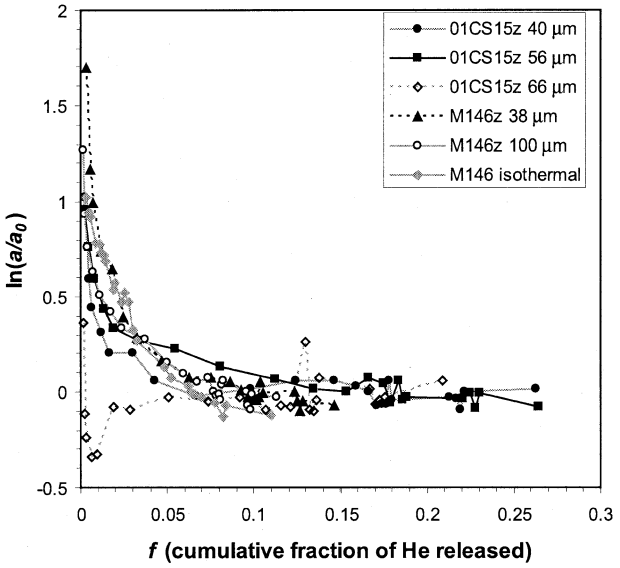

Fig. 9. Ln(a/a_0) vs. cumulative fraction of He released in step-heating experiments. See text for derivation. This plot shows changes in apparent diffusivity as a function of total fraction of gas released. For most samples, including the experiment involving multiple isothermal steps at low temperature, ln(a/a_0) reaches close to zero by ~5–7% gas released, showing that changes in apparent diffusivity unrelated to temperature are negligible after this. In the context of a multidomain diffusion model, both the value of the early ln(a/a_0) and the shape of its approach to zero are a function of relative gas fractions and diffusivities of the domains.

long-term residence at low temperature, appears to be required to significantly affect He diffusion properties and ages for zircon.

It is possible that the effects of radiation damage on Arrhenius plots for He diffusion experiments may be more complex than radiation dosage of a bulk grain would predict, however. Rather than actually changing bulk diffusion parameters in step-heating experiments by progressively annealing radiation damage, it is possible that multiple diffusion domains created by radiation damage may sequentially degas during step heating. This multidomain behavior would lead to apparently decreasing diffusivity in Arrhenius plots, as observed for zircon.

Radiation damage may be heterogeneously distributed at a range of scales. Damage due to α particle recoil occurs within 15–20 μm of parent nuclides, damage from intermediate daughter recoil occurs within 20–50 nm of parents, and much rarer (10^{-6} times less abundant) fission recoil damage is manifested as tracks ~0.5 by 15 μm. Uranium and Th are also typically heterogeneously distributed in zircon, commonly in self-similar oscillatory zonation over a range of scales (Fowler et al., 2002). These considerations suggest, and spectroscopic and microscopic studies confirm (Sahama, 1981; Chakoumakos et al., 1987; Smith et al., 1991; Lee and Trump, 1995; Nasdala et al., 2001), that radiation damage is heterogeneous and occurs over a range of length-scales. If He diffusivity scales with radiation damage intensity, then individual crystals would be expected to possess regions with different diffusivities, each characterized by different length-scales that reflect different levels of damage or intracrystalline U-Th zonation. In any case, local high-damage zones would be expected to have relatively high diffusivity (although see Farley, 2000, for different interpretation of effects of fission-track damage on He diffusion in apatite), which may exert an apparently large effect on Arrhenius plots in the early stages of degassing. In this case, the effects of radiation damage would resemble, and possibly be both empirically and mechanistically indistinguishable from, those of He release from multiple diffusion domains with varying size or other properties.

4.3. Multidomain Models

Some of the most salient features of multidomain diffusion models have been pointed out in studies of K-feldspar by Lovera et al. (1989, 1991, 1997, 2002). For the specific case of He diffusion from titanite, Reiners and Farley (e.g., Fig. 5 of 1999) also showed general effects of several endmember types of two-domain configurations. One of the most general results is that, assuming no interaction between domains (i.e., no "nesting"), mixtures of domains with varying E_a, D_0, or a, will result in Arrhenius plots with apparently decreasing diffusivity at a given temperature during step-heating, which is the phenomenon observed in our samples.

Here we take the approach of forward modeling Arrhenius plots of our experiments with two- and three-diffusion domain models. Although highly simplified, this allows us to assess the importance of the observed deviations in Arrhenius plots from predicted single-domain behavior, in the context of parameters that can be varied for multidomain models. Variable parameters for each of the domains are E_a, D_0, size a, and fraction of gas in each domain ϕ. To calculate synthetic Arrhenius plots for our heating schedule, we predicted D/a^2 for each domain and each heating step from the Arrhenius equation, then calculated fraction degassed from each domain using inverted versions of the step-heating approximation equations of Fechtig and Kalbitzer (1966) (solved for f instead of D_0/a^2). Gas released from each domain was then recombined into an apparent cumulative degassed fraction f for the aggregate of domains, by weighting each domain according to its assumed ϕ.

Given the large number of variable parameters in a multidomain diffusion model, forward modeling cannot constrain the entire range of configurations that could produce Arrhenius plots as in Figure 1. However, consideration of several endmember cases allows useful insight. The most important controls on the overall "shape" of the Arrhenius plot, and the ln(a/a_0) vs. f plot, are the effective diffusivity of each domain at a given temperature, D/a^2, and the relative proportions of gas contained in each domain, ϕ. The effects of effective diffusivity of each domain can be examined completely by casting variations in D/a^2 as simply varying a, although in reality this could correspond to changes in either or both scale-independent diffusivity D, or domain size a. Average E_a and D_0 derived from the post-high-T heating steps of the diffusion experiments were used in all the models. These specific values are inconsequential compared with variations in a and ϕ.

Figure 10 shows the effects of variations in D/a^2 and ϕ between domains for a series of two-domain models. In the first set of models, each domain contains 50% of the total gas, a of the large domain is 100 μm, and a of the small domain varies between 0.5 and 20 μm. The second and third sets are similar except gas proportions are 80:20 and 98:2, respectively. Each

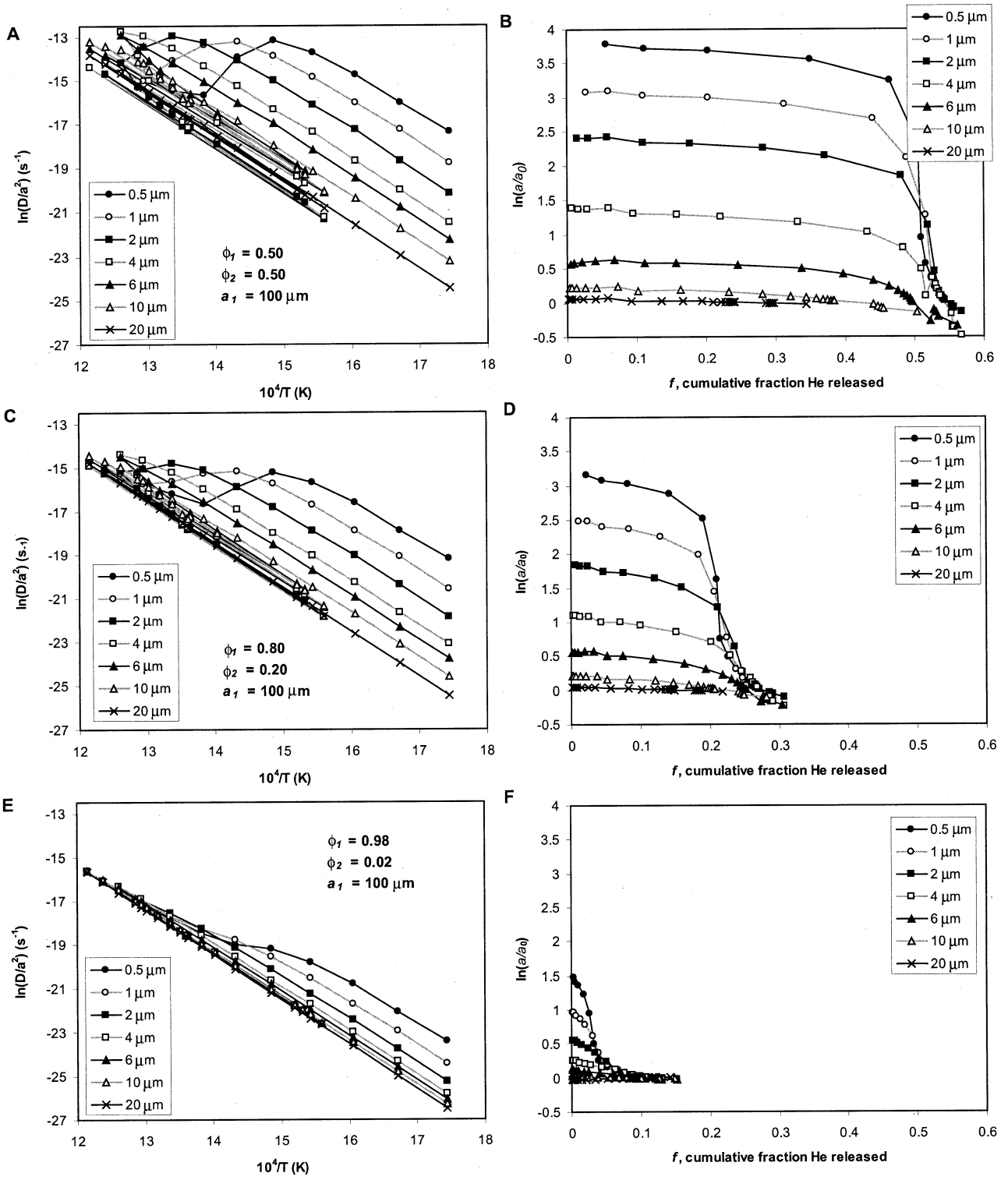

Fig. 10. Arrhenius and ln(a/a_0) plots from synthetic diffusion data predicted from two-domain diffusion models. See text for details of modeling. In all models, 1) E_a and D_0 of all domains are 168 kJ/mol (40 kcal/mol) and 0.6 cm^2/s, respectively, and 2) the size of domain 1 (a_1) is 100 μm, and the size of domain 2 (a_2) varies from 0.5 to 20 μm (see inset keys). The relative proportions of gas in each domain are listed in A, C, and E, as σ_1 and σ_2 and apply to each of the plots to the right as well. Although no two-domain model closely reproduces the appearance of Arrhenius and ln(a/a_0) plots for zircon (Figs. 2, 9), the ones that come closest have small proportions of gas (ϕ<2–3%) in domains with effectively high diffusivity (in this model, small size; a = 0.5–1 μm).

model predicts a decrease in D/a^2 with progressive degassing, although this decrease is difficult or impossible to resolve as the contrast in domain sizes becomes small (<factor of 10). In most cases, several heating steps are required to completely degas the small (or less retentive) domain. This leads to two subparallel trends, one for early and one for later steps. The point in the experiment at which the small domain is fully depleted is primarily a function of its fractional gas content ϕ. The vertical distance between the early and later step trends is mainly a function of the size of the small domain a relative to the larger one.

Of these models, the synthetic Arrhenius trends that appear most similar to those of the actual experiments are those in which both the gas content ϕ and size a of the small domain are very small, less than 0.02 and less than ~2 μm, respectively (Fig. 10E). If a of the small domain is larger than this (i.e., smaller contrast between the small and large domain sizes), the Arrhenius trend of the early steps is subparallel to later steps for too many steps, and does not display the shallower slope merging with the later trend, as in the real experiments (Fig. 1). Even in the case of the smallest a and lowest ϕ, the early trend is subparallel to the later trend for the first 3–4 steps, unlike the more or less continuously sloping trend of the real experiments. If ϕ of the small domain is larger than ~0.02, the initital steps are displaced to D/a^2 that are far too high relative to the trend of later steps.

This last point is more easily seen in the $\ln(a/a_0)$ plots. In the first two sets of models, either there is very little change in $\ln(a/a_0)$ in the model run, or the change occurs at cumulative degassing (f) far higher than observed in the real experiments (Figs. 9, 10), which in fact show a relatively continuous decrease in $\ln(a/a_0)$ through $f \sim 0.05$–0.10. In the models with small ϕ, there is a more steady decrease in $\ln(a/a_0)$ through $f \sim 0.05$–0.10, but in these two domain models there still is a step-like decrease, especially for the runs with lowest a of the small domain (Fig. 10F).

Although we have not explored the full range of parameter space, these examples and those of many other forward models not shown here suggest that the two-domain model that produces non-Arrhenius behavior in early degassing steps most similar to that observed for He diffusion from zircon involves a small proportion of gas ($\phi < 0.02$) in a relatively small domain ($a < 0.5$ μm if the other domain is 100 μm). All two-domain models with this configuration, however, predict step-like changes in Arrhenius plots and $\ln(a/a_0)$ that are unlike the real experiments, because of the discrete step associated with degassing the small domain. This suggests that a continuum of domains with increasingly smaller proportions of gas in increasingly smaller domains would reproduce the observations better, as is seen in K-feldspar multidomain models. Without developing an actual continuum model, we note that a three-domain model (Fig. 11) with such characteristics produces a significantly better fit, and is in fact nearly indistinguishable from the experiments themselves. This model involves large, intermediate, and small domains with $a = 100$ (or 60 μm), 4 μm, and 0.2 μm, with $\phi = 0.970$, 0.025, and 0.005, respectively.

The most important result of this modeling is that the non-Arrhenius behavior of He diffusion from zircon in the early stages of step-heating experiments can be simply explained by a multidomain diffusion model in which only a small proportion of gas resides in small domains. The effect of these small domains on the bulk diffusivity of a zircon crystal would be minimal. For the three-domain model above with $a = 60$ μm for the largest domain, the effective closure temperatures of each domain (for a cooling rate of 10°C/myr) would be 183°C, 132°C, and 90°C. For a bulk crystal in which these domains represented 97%, 2.5%, and 0.5% of the gas, respectively, the weighted closure temperature would be 182°C. In the context of this model, even if the smaller domains represented a significantly higher fraction of gas (up to 10–20%, for example), the bulk closure temperature of a crystal would not be expected to vary by more than that caused by variation in diffusion parameters derived from the post-high-T heating steps of different experiments (Table 2). As suggested previously for titanite (Reiners and Farley, 1999), if the origin of non-Arrhenius behavior of He diffusion from zircon in early low-T heating steps has an origin in some mechanism producing multiple domains, or multidomain-like effects (such as might qualitatively arise from a wide range of sources like anisotropy, spatially heterogeneous radiation damage, or multipath diffusion), these effects are essentially negligible for the thermochronometric potential of zircon.

4.4. Thermochronologic Data

In general, replicate zircon He ages are concordant with K-feldspar cooling models at the calculated zircon closure temperatures (Fig. 12). Mean zircon He ages of two samples (Tracy Arm and Southwest Arm) are highly concordant with K-feldspar cooling models (Figs. 6, 8, 12). The Tracy Arm sample has both replicate and mean ages within 2% of the Ar model at the same temperature. The Southwest Arm pluton also has a mean age that is indistinguishable from the Ar model, although replicate ages scatter about the mean as much as 8%. Unfortunately, the Ar cooling model of sample KFR7 from the Te Kinga pluton does not extend to sufficiently low temperatures to directly compare with the zircon He age. However, linear extrapolation of the KFR7 cooling model encompasses the measured zircon He ages. Finally, although three out of five zircons from sample TK7 yielded He ages that overlap the K-feldspar cooling model, two crystals are significantly older, and as a whole this sample shows relatively poor reproducibility and a mean that is ~15–25% older than the Ar cooling model at the inferred closure temperature.

Before addressing reproducibility, we point out that although there is good agreement between zircon He ages and Ar cooling models for the Tracy Arm and Southwest Arm samples, this only qualitatively supports the zircon He closure temperature of 170–190°C inferred from diffusion experiments. Assuming an uncertainty of 4% (1σ of Fish Canyon Tuff reproducibility), the inferred closure temperatures of both the Southwest Arm and Tracy Arm samples could be as high as 225°C and 278°C, respectively, and still overlap the Ar cooling models at those temperatures (Figs. 6 and 8). The lowest temperatures reached by the acceptable parts of the Ar cooling models, 102°C and 157°C, respectively, would also overlap at the 4% level with the measured zircon He ages. If the cooling rate of these rocks were slower, there would be better resolution of time–temperature relationships and opportunity to more tightly constrain the

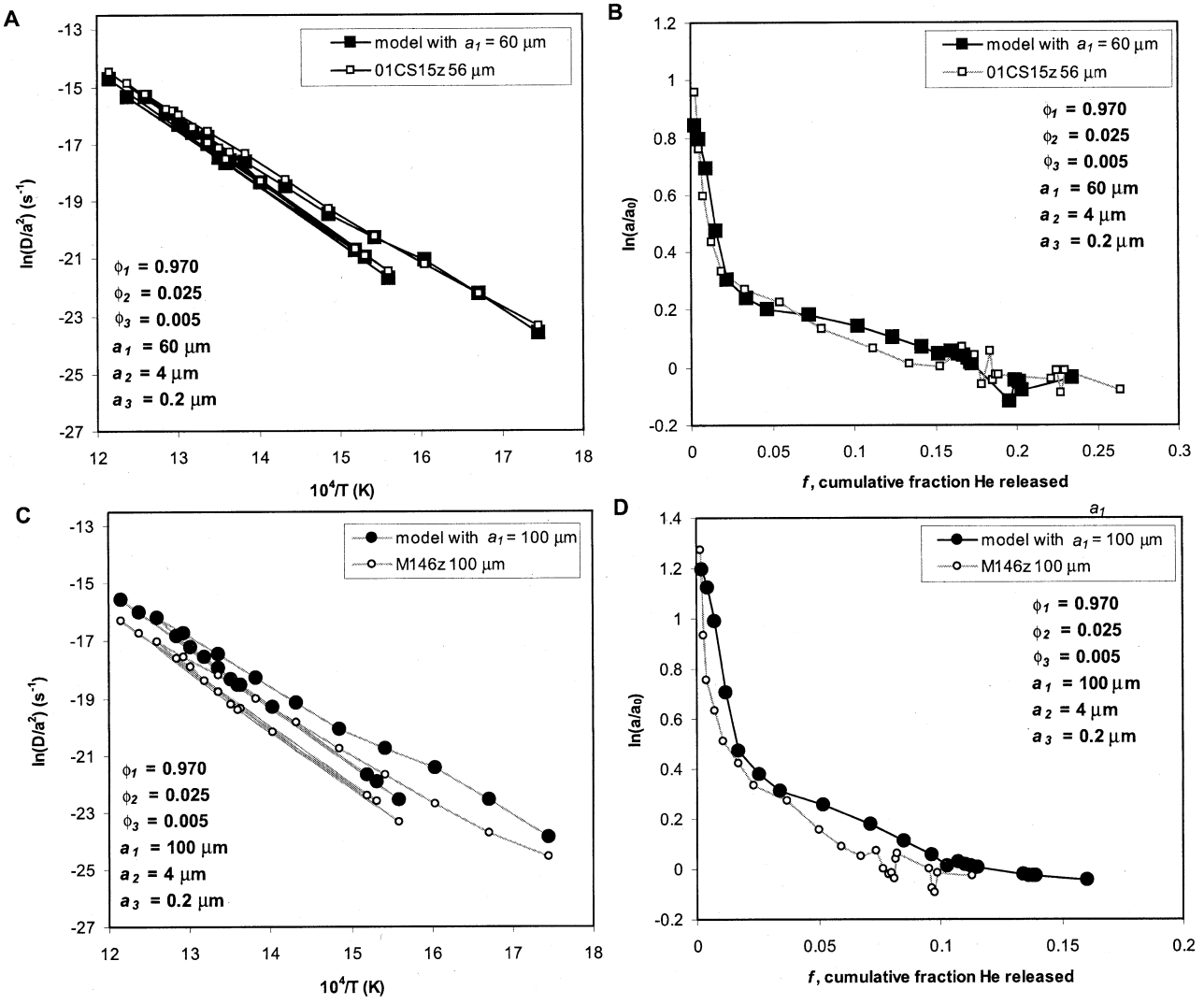

Fig. 11. Arrhenius and ln(a/a_0) plots from synthetic diffusion data predicted from three-domain diffusion models that reproduce observed data for natural zircons. Trends from two real experiments are shown for comparison. Assuming that only 2.5% and 0.5% of gas reside in domains that are 25 times and 200 times smaller than the bulk grain, respectively, and using average E_a and D_0 derived from post-high-T portions of the diffusion experiments, closely reproduces the observed features.

zircon He T_c. At least in the case of apatite, lower cooling rates often lead to poorer reproducibility, however, because small differences in diffusivity from a variety of causes can greatly magnify age differences (Reiners and Farley, 1999; House et al., 2001). Despite these concerns, the overall agreement between the two thermochronologic systems is relatively good, and suggests that the underlying assumptions are robust (Fig. 12).

The 8% (2σ) reproducibility of Southwest Arm zircon ages may be partly due to the small size of these crystals (25–37 μm in radius). The average α-ejection correction for these samples is large; average F_T (Farley, 2002) is 0.65, and as low as 0.61. Random error in measurement of tetragonal width as low as 4 (m could lead to apparent age differences between crystals as high as ~5%. However, this is still less than the 8% observed for the Southwest Arm, and much less than the age scatter for TK7.

4.5. U-Th Zonation

One potentially important source of age scatter in He dating in general is heterogeneous intracrystalline U and Th distribution (zonation) because, as typically applied, α-ejection corrections assume homogeneous U-Th distribution. The direction and magnitude of age bias resulting from the U-Th zonation depends on the style and extent of the zonation (Farley et al., 1996; Meesters and Dunai, 2002). This has been shown experimentally by Tagami et al. (2003) for zircons from the Tardree tuff, which have high U-cores and yield ages as much as 20% higher than the U/Pb age.

We examined zonation of trace elements in zircons from the Te Kinga and Southwest Arm plutons using electron microprobe analyses and imaging (back-scattered electron [BSE] and cathodoluminesence [CL] imaging). Southwest Arm pluton zircons showed very little obvious zonation with these tech-

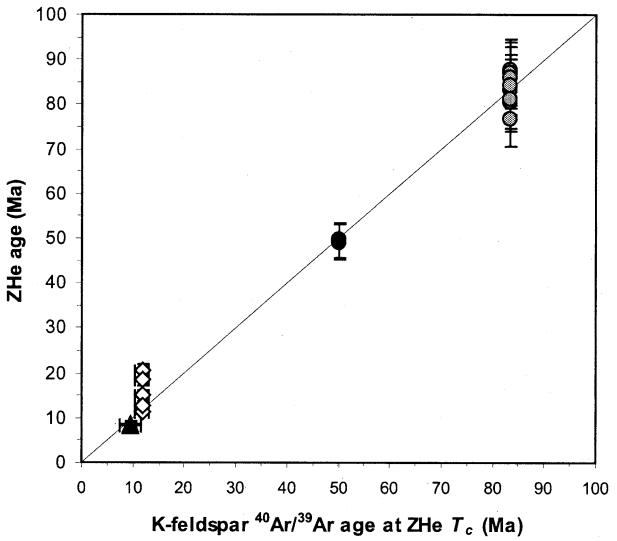

Fig. 12. Single-grain zircon (U-Th)/He ages plotted against K-feldspar ^{40}Ar/^{39}Ar age (or extrapolated age) at the average closure temperatures for each sample (170–191°C in these samples). In general, zircon He ages match predicted ages from K-feldspars, although replicates show an 8% standard deviation in the Southwest Arm pluton (gray circles), and two grains have significantly older ages in the TK7 Te Kinga sample (white diamonds). Other symbols: black circles: Holkham Bay/Tracy Arm (southeast Alaska); black triangles: KFR7 Te Kinga pluton.

niques, but approximately one-quarter of grains from both Te Kinga samples (TK7 and KFR7) showed striking variation in BSE and CL contrast within single crystals (Fig. 13), with a variety of zonation types. Electron microprobe and laser-ablation ICP-MS analyses confirm that high BSE and low CL intensity zones have relatively high U-Th, although the magnitude of U-Th concentration contrast does not scale consistently with image contrast in BSE or CL. In these samples, the most commonly observed types of zonation are cores with U-Th concentrations up to 20–30 times higher than rims, and pyramidal terminations with U-Th concentrations between 2 and 30 times higher than the rest of the crystal. These zonation types would cause too-old and too-young α-ejection corrected ages, respectively.

Although the zircons shown in Figure 13 are examples of the most extreme zonation we observed in these samples, and these particular grains are smaller than typically analyzed ones, they suggest that U-Th zonation, and its indirect effect on accuracy of the α-ejection correction, may be a very significant source of the age scatter observed in some of these samples. To estimate the magnitude of age bias caused by the U-Th zonation observed in Figure 13, we can approximate the zonation as a step-function in U concentration contrast of factor n, located at distance r from the rim of the crystal. To generalize the results, we calculated α-ejection corrections (F_T of Farley et al., 1996, using average ^{238}U stopping distance) for spheres with radii of 72 μm, with equivalent surface area to volume ratios, and therefore similar F_T, as tetragonal prisms with half-widths of 60 μm.

Figure 14 shows relative inaccuracies of α-ejection corrections and their effect on calculated ages as a function of r and n. Rims depleted in U-Th by factors of 2–20 (i.e., n = 0.5–0.05, or high U-Th cores) lead to α-ejection corrections, and thus ages, that are too high by ~5–20%. For depleted rims (i.e., enriched cores), age bias is maximized for rims that are ~10–20 μm thick. Figure 14 also shows that the magnitude of effects of rim depletion on corrected ages drops off quickly for thinner rims, but remains relatively high for thick rims. For rims less than ~2 microns thick, depletion factors as high as 20–30 result in no more than ~5% inaccuracy. In contrast, rims that are *enriched* in U-Th by factors of 5–20 lead to α-ejection corrections and ages that are too low by as much as 15–30%. For enriched rims, inaccuracies are maximized for rims between ~4–9 μm thick. The magnitude of effects of rim enrichment on corrected ages drops off quickly for thicker rims, but remains relatively high for thin rims. For example, enriched rims only 1 μm thick produce inaccuracies as high as 7% for a fivefold enrichment, and 20% for a 20-fold enrichment.

If dated crystals from the TK7 sample (Fig. 4) had zonation like that in the TK7 zircons with high U-Th cores (Fig. 13), this could explain the outlying old ages on several of the crystals, compared with the ages on the other zircons that are concordant with the K-spar cooling model (Fig. 4). One of the TK7 grains in Figure 13 shows U enrichment of at least a factor of 20–30 in the core, and a U-depleted rim between 5 and 20 μm thick. Assuming an average rim thickness of 12 μm, this would be expected to generate an age 18% too high. Without knowing the actual zonation in the specific dated crystals, it is not possible to conclude with certainty that U-depleted rims as observed in some of the crystals are responsible for the older single-grain ages on some replicates. However, the poor reproducibility of ages on this sample (1σ of 24%) is clearly consistent with biased α-ejection corrections arising from a population of grains with occasionally strong U-enriched cores, as seen in Figure 13.

Although replicate analyses of three single zircon crystals from sample KFR7 reproduced well, several of the grains examined by electron microprobe imaging showed significant U-Th zonation (Fig. 13). To test the hypothesis that intracrystalline U-Th zonation leads to inaccurate ages via the α-ejection correction, we used laser-ablation inductively coupled plasma mass spectrometry (LA-ICP-MS) to characterize rim-to-core U and Th zonation in single zircon crystals from KFR7. For this we used a 213-nm laser with a 40-μm spot and a drilling rate of 0.6 μm/s. Large grain fragments of zircons with homogeneous U concentrations were used for standardization and to correct for depth-dependent U/Zr (which is negligible compared with intracrystalline U variation), and multiple ages on depth-profiled Fish Canyon Tuff zircons were used to demonstrate that laser ablation does not affect (U-Th)/He ages (Hourigan et al., 2003).

Figure 15 shows the U concentration depth-profile of a zircon from this sample (BUKFR7zH) with a fivefold exponential core-to-rim increase. Following laser profiling, we performed a routine (U-Th)/He age determination on the crystal. Assuming homogeneous U-distribution and a typical α-ejection correction, the age of this crystal is 7.55 Ma, ~10% younger than the mean of the other three single-grain KFR7 ages. To quantify the effect of the observed zonation on α-ejection corrected age, we calculated two different α-ejection corrections for a sphere with the equivalent surface area to volume ratio as the crystal: one assuming homogeneous U concentration (the standard F_T, here called HAC, for homogeneous

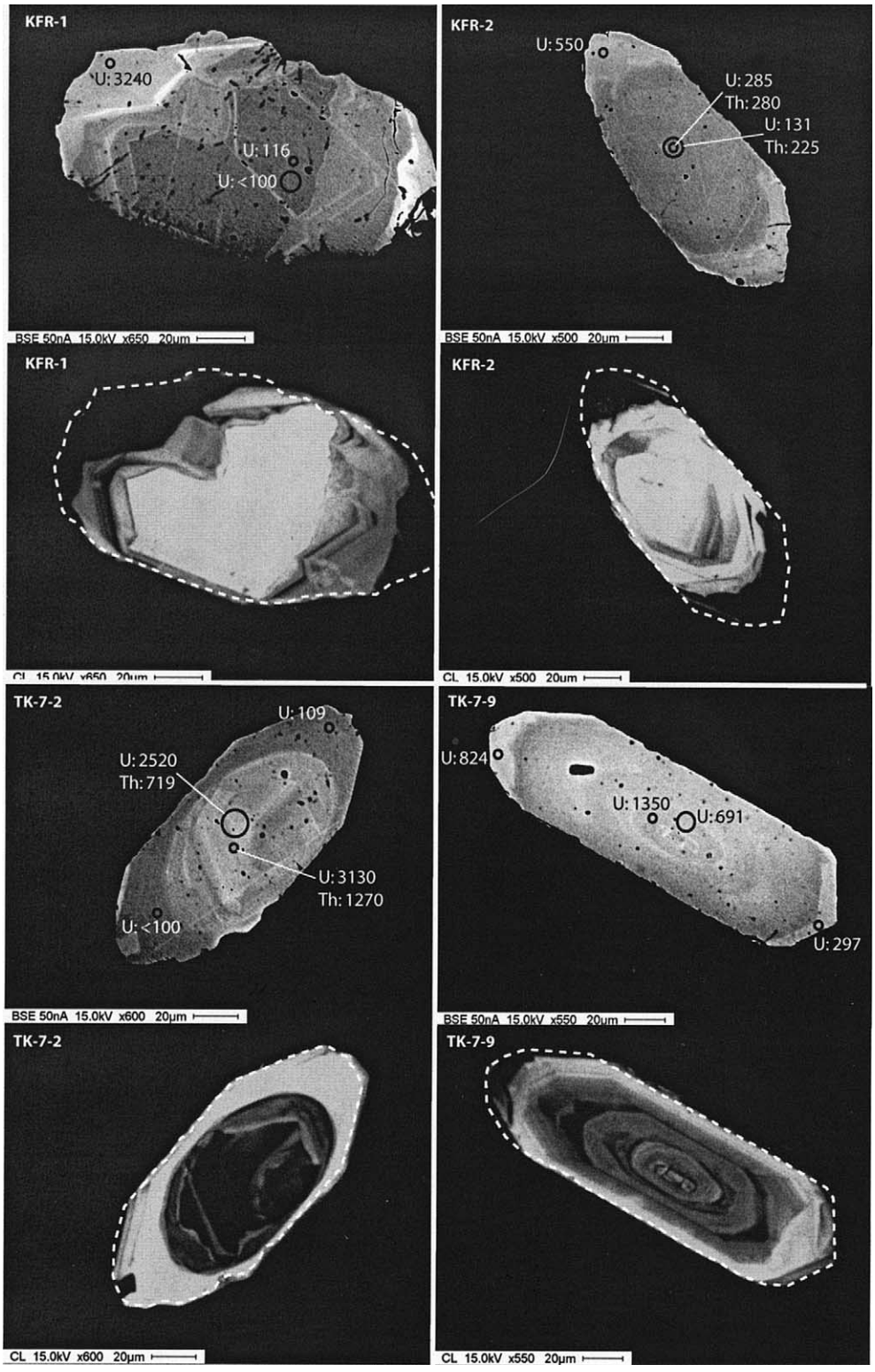

Fig. 13. Back-scattered electron (BSE) and cathodoluminesence (CL) images of zircons from the Te Kinga pluton. Bright contrast in BSE and dark contrast in CL are relatively high U-Th zones. Locations of spot analyses by electron microprobe, and concentrations (in ppm) are shown for U and Th, where concentrations were above detection limit (100 ppm). Analytical uncertainty is estimated to be ~100 ppm on these analyses. About one-quarter to one-third of zircons from these two samples show strong zonation that would be expected to introduce significant age scatter, via inaccurate α-ejection corrections.

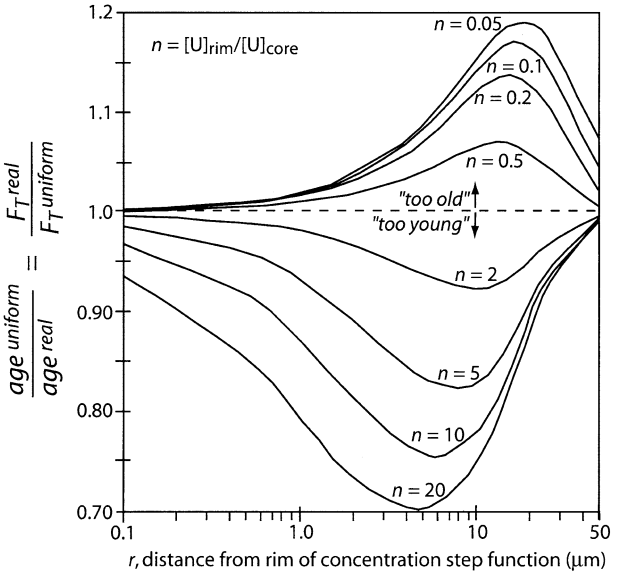

Fig. 14. Magnitude of inaccuracies in α-ejection corrections resulting from U zonation, calculated for the average stopping distance of α's produced from ^{238}U in zircon (16.68 μm). "Uniform" and "real" correspond to values that would be calculated assuming uniform U-Th concentrations in the dated crystal, or to those calculated accounting for real zonation. Calculations are for a sphere with a radius of 72 μm, which has an equivalent surface area to volume ratio, and thus approximately equivalent α-ejection correction, as that of a simplified zircon with tetragonal prism morphology, prism half-width of 60 μm, and 2:1 aspect ratio. Zonation is represented as a step function of concentration with magnitude n (n = ratio of U concentrations in rim to those in core), located at distance r (microns) from the rim of the crystal. Maximum inaccuracies for U-enriched and -depleted rims occur for rims 4–9 μm, and 10–20 μm thick, respectively. For thin crystal rims (<5–10 μm), U-enrichment generates much higher inaccuracies than depletion for a given concentration contrast.

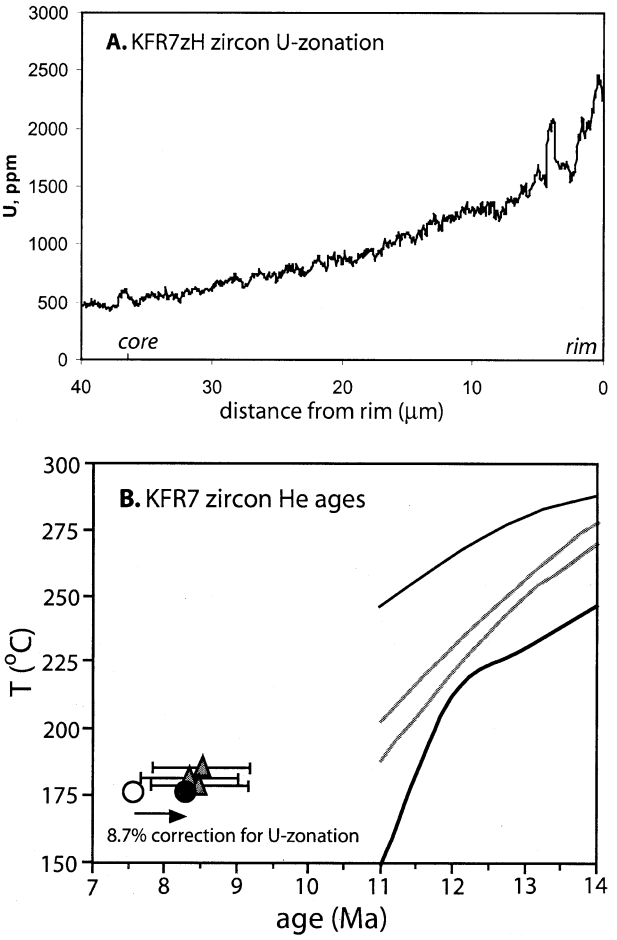

Fig. 15. (A) U concentration in a rim-to-core profile perpendicular to the c-axis in a single TK7 zircon, measured by LA-ICP-MS. This grain has a half-width of 36 μm, and shows a fivefold exponential increase in U concentration from core to rim. (B) Low-temperature portion of K-feldspar ^{40}Ar/^{39}Ar cooling model, with single-grain zircon He ages shown in Figure 4, and ages of depth-profiled grain assuming homogeneous U distribution (white circle) and observed core-to-rim U zonation (black circle) shown in A (see text).

α-ejection correction), and one assuming concentric U zonation of the style and extent observed in Figure 15A (here called ZAC, or zonation α-ejection correction). ZAC was calculated using a model with 1000 spherical shells with local α-ejection of each shell weighted by observed core-to-rim concentrations imposed concentrically on the sphere (results for homogeneous and prescribed function zonations agree within <1% with those of Farley et al., 1996). The ZAC to HAC ratio (0.913 in this case) is then equal to the ratio of HAC-age to ZAC-age. The raw age on zircon BUKFR7zH was then corrected for the effects of α-ejection by an F_T that is a factor of 0.913 less than that which would be applied assuming homogeneous U distribution. This results in an 8.7% increase in the α-ejection corrected age, bringing it into concordance with the other zircon ages of this sample (Fig. 15B). This suggests that LA-ICP-MS depth profiling may provide a useful tool not only for screening out crystals with extensive U-Th zonation, but also for determination of U-zonation-specific α-ejection corrections, which may significantly improve the precision and accuracy of single-grain (U-Th)/He ages.

In contrast to the Te Kinga samples, both electron microprobe and fission-track imaging/analyses show that significant U-Th zonation is rare in zircons from the Southeast Alaska and Southwest Arm pluton samples studied here. Importantly, these samples yielded zircon He ages that are the most concordant with K-spar cooling models. Together with the results on zircon BUKFR7zH, this suggests that intracrystalline zonation of U and Th is probably the most significant hurdle to accurate and reproducible zircon (U-Th)/He ages, but one that may be addressed by LA-ICP-MS depth profiling before dating.

5. CONCLUSIONS

Step-heating He diffusion experiments on zircons, including homogeneous interior fragments of large gem-quality crystals with old ages and high U-Th contents, suggest an E_a = 163–173 kJ/mol (39–41 kcal/mol), and D_0 = 0.09–1.5 cm^2/s, with an average E_a of 169 ± 3.8 kJ/mol (40.4 ± 0.9 kcal/mol) and average D_0 of $0.46^{+0.87}_{-0.30}$ cm^2/s. For a typical exhumation-related cooling rate of 10°C/myr and crystal half-widths of 60 μm, these parameters yield closure temperatures in the range of 171–196°C. Non-Arrhenius behavior of He diffusion in the early stages of step-heating experiments could have a number of physical origins, but its effects can be easily modeled as a

small proportion (2–3%) of gas degassing from domains with effectively higher diffusivity than the bulk grain. If this high diffusivity is due primarily to size variations, the domains are 25 to 200 times smaller than the bulk grain. This suggests that departures from linearity in early stages of Arrhenius trends as observed in this case and for titanite (and possibly other minerals) are insignificant for bulk closure temperature and thermochronologic constraints.

Comparison of single crystal zircon (U-Th)/He ages with intermediate- to low-temperature cooling models from $^{40}Ar/^{39}Ar$ step-heating spectra shows good agreement in most cases. Although the relatively rapid cooling inferred from some of the Ar cooling models does not allow precise empirical tests of the zircon He closure temperature beyond consistency within ~100–250°C, in two out of three cases where K-feldspar cooling trends overlap inferred zircon He closure temperature, He ages fall well within 1σ of Ar constraints. In one case, single crystal ages show a large scatter and higher mean than predicted by the Ar cooling model. Microimaging and LA-ICP-MS demonstrates that some zircons from this pluton have strong intracrystalline zonation and thus that the homogeneous U-Th assumption required for typical α-ejection corrections may not always hold. However, characterization of intracrystalline U-zonation by LA-ICP-MS depth profiling, followed by (U-Th)/He dating with a zonation-specific α-ejection correction suggests that this method may provide a useful routine procedure for improving the accuracy and precision of He dating.

Acknowledgments—We thank Peter Zeitler, Mark Harrison, and two anonymous reviewers for helpful comments. We acknowledge Jeremy Hourigan, Terry Plank, and Katherine Kelley for help with LA-ICP-MS depth-profiling, Harold Stowell for providing Alaskan samples, Tod Waight for providing Hohonu Batholith samples, Hunter Hickes for analysis of some of the Alaskan samples, and Jim Eckert for electron microprobe assistance. This project was supported by NSF. Acknowledgment is also made to the Donors of the American Chemical Society Petroleum Research Fund for support of this research.

Associate editor: M. Harrison

REFERENCES

Allibone A. H. (1991) Volcanogenic and granitoid rocks from northwest Stewart Island. *New Zealand J. Geol. Geophys.* **34,** 35–50.

Allibone A. H. and Tulloch A. J. (1997) Metasedimentary, granitoid and gabbroic rocks from central Stewart Island, New Zealand. *New Zealand J. Geol. Geophys.* **40,** 53–68.

Armstrong R. L., Taubeneck W. H., and Hales P. O. (1977) Rb-Sr and K-Ar geochronometry of Mesozoic granitic rocks and their Sr isotopic composition, Oregon, Washington, and Idaho. *Geol. Soc. Am. Bull.* **88,** 397–411.

Arnaud N. O. and Kelley S. P. (1997) Argon behaviour in gem-quality orthoclase from Madagascar: Experiments and some consequences for $^{40}Ar/^{39}Ar$ geochronology. *Geochim. Cosmochim. Acta* **61,** 3227–3255.

Aronson J. L. (1965) Reconnaissance rubidium-strontium geochronology of New Zealand plutonic and metamorphic rocks. *New Zealand J. Geol. Geophys.* **8,** 401–423.

Aronson J. L. (1968) Regional geochronology of New Zealand. *Geochim. Cosmochim. Acta* **32,** 667–697.

Brandon M. T. and Vance J. A. (1992) New statistical methods for analysis of fission track grain age distributions with applications to detrital zircon ages from the Olympic subduction complex, western Washington State. *Am. J. Sci.* **292,** 565–636.

Cebula G. T., Kunk M. J., Mehnert H. H., Naeser C. W., Obradovich J. D., and Sutter J. F. (1986) The Fish Canyon Tuff, a potential standard for the ^{40}Ar-^{39}Ar and fission-track dating methods (abstract). *Terra Cognita (6th Int. Conf. on Geochronology, Cosmochronology and Isotope Geology)* **6,** 139.

Chakoumakos B. C., Murakami T., Lumpkin G. R., and Ewing R. C. (1987) Alpha-decay-induced fracturing in zircon: The transition from the crystalline to the metamict state. *Science* **236,** 1556–1559.

Crawford M. L., Hollister L. S., and Woodworth G. J. (1987) Crustal deformation and regional metamorphism across a terrane boundary, Coast plutonic complex, British Columbia. *Tectonics* **6,** 343–361.

Damon P. E. and Kulp J. L. (1957) Determination of radiogenic helium in zircon by stable isotope dilution technique. *Trans. Am. Geophys. U.* **38,** 945–953.

Dodson M. H. (1973) Closure temperature in cooling geochronological and petrological systems. *Contrib. Mineral. Petrol.* **40,** 259–274.

Donelick R. A (1986) Mesozoic-Cenozoic thermal evloution of the Atlin terrane, Whitehorse trough and Coast Plutonic Complex from Atlin, British Columbia to Haines as revealed by fission-track geothermometry techniques. M.Sc. thesis, Rensselaer Polytechnic Institute, Troy, New York, 167 pp.

Farley K. A. (2000) Helium diffusion from apatite: General behavior as illustrated by Durango fluorapatite. *J. Geophys. Res.* **105,** 2903–2914.

Farley K. A. (2002) (U-Th)/He dating: Techniques, calibrations, and applications. *Mineral Soc. Am. Rev. Mineral. Geochem.* **47,** 819–844.

Farley K. A. and Stockli D. F. (2002) (U-Th)/He dating of phosphates: Apatite, monazite, and xenotime. *Mineral Soc. Am. Rev. Mineral. Geochem.* **48,** 559–577.

Farley K. A., Wolf R. A., and Silver L. T. (1996) The effects of long alpha-stopping distances on (U-Th)/He ages. *Geochim. Cosmochim. Acta* **60,** 4223–4229.

Farley K. A., Reiners P. W., and Nenow V. (1999) An apparatus for measurement of noble gas diffusivities from minerals in vacuum. *Analyt. Chem.* **71,** 2059–2061.

Farley K. A., Rusmore M. E., and Bogue S. W. (2001) Post-10. Ma uplift and exhumation of the northern Coast Mountains, British Columbia. *Geology* **29,** 99–102.

Fechtig H. and Kalbitzer S. (1966) The diffusion of argon in potassium bearing solids. In *Potassium-Argon Dating* (eds. O. A. Schaeffer and J. Zahringer), pp. 68–106. Springer-Verlag, New York.

Fitzgerald J. D. and Harrison T. M. (1993) Argon diffusion domains in K-feldspars I: Microstructures in MH-10. *Contrib. Mineral. Petrol.* **113,** 367–380.

Foster D. A., Kohn B. P. and Gleadow A. J. W.(1996) Sphene and zircon fission track closure temperatures revisited: Empirical calibrations from $^{40}Ar/^{39}Ar$ diffusion studies on K-feldspar and biotite. International Workshop on Fission Track Dating Abstracts, August 26–30, University of Gent, Gent 37.

Fowler A., Prokoph A., Stern R., and Dupuis C. (2002) Organization of oscillatory zoning in zircon: Analysis, scaling, geochemistry, and model of a zircon from Kipawa, Quebec, Canada. *Geochim. Cosmochim. Acta* **66,** 311–328.

Gallagher K., Brown R., and Johnson C. (1998) Fission track analysis and its applications to geological problems. *Ann. Rev. Earth Planet. Sci.* **26,** 519–572.

Garver J. I. (2002) Discussion. "Metamictisation of natural zircon: Accumulation versus thermal annealing of radioactivity-induced damage" by Nasdala et al. *2001 (Contrib. Mineral. Petrol. 141, 125–144). Contrib. Mineral. Petrol.* **143,** 756–757.

Gehrels G. E., McClelland W. C., Samson S. D., Patchett P. J., and Brew D. (1991) U-Pb geochronology of Late Cretaceous and early Tertiary plutons in the northern Coast Mountains batholith. *Can. J. Earth Sci.* **28,** 899–911.

Harper C. T. (ed.) (1973) *Geochronology: Radiometric Dating of Rocks and Minerals,* Dowden, Hutchinson & Ross, 469 pp.

Harrison T. M., Armstrong R. L., Naeser C. W., and Harakal J. E. (1979) Geochronology and thermal history of the Coast Plutonic Complex, near Prince Rupert, British Columbia. *Can. J. Earth Sci.* **16,** 400–410.

Heizler M. T., Appelt R., Perry F. V., Crowe B. M., and Peters L. (1999) The age of Lathrop Wells volcanic center: An $^{40}Ar/^{39}Ar$ dating investigation. *J. Geophys. Res.* **104,** 767–804.

Hickes H. J., Reiners P. W., Donelick R. A. and Stowell H. H. (2000). Apatite and zircon (U-Th)/He thermochronometry of the northern Coast Mountains, Southeast Alaska. *Eos Trans., Am. Geophys. U.* **81,** Fall Meet. Suppl., Abstract T51.C-10.

Hickes H. J. (2000). Apatite and zircon (U-Th)/He thermochronology of the northern Coast Mountains, Southeast Alaska. M.Sc. thesis, Washington State University.

Hourigan J. K., Reiners P. W., Nicolescu S., Plank T., and Kelley K. (2003) Zonation-dependent alpha-ejection correction by laser ablation ICP-MS depth profiling: Toward improved precision and accuracy of (U-Th)/He ages. *Eos Trans. AGU* **84**(46), Fall Meet. Suppl., Abstract V22G-04.

House M. A., Wernicke B. P., and Farley K. A. (2001) Paleo-geomorphology of the Sierra Nevada, California, from (U-Th)/He ages in apatite. *Am. J. Sci.* **301,** 77–102.

Hurford A. J. (1986) Cooling and uplift patterns in the Lepontine Alps, South Central Switzerland and an age of vertical movement on the Insubric fault line. *Contrib. Mineral. Petrol.* **92,** 413–427.

Hurley P. M. (1952) Alpha ionization damage as a cause of low helium ratios. *Trans. Am. Geophys. U.* **33,** 174–183.

Hurley P. M. and Fairbairn H. W. (1953) Radiation damage in zircons: A possible age method. *Bull. Geol. Soc. Am.* **64,** 659–674.

Hurley P. M., Larsen E. S., Jr., and Gottfried D. (1956) Comparison of radiogenic helium and lead in zircon. *Geochim. Cosmochim. Acta* **9,** 98–102.

Johnson K., Barnes C. G., and Miller C. A. (1997) Petrology, geochemistry, and genesis of high-Al tonalite and trondjemites of the Cornucopia stock, Blue Mountains, Northeastern Oregon. *J. Petrol.* **38,** 1585–1611.

Kamp P. J. J., Green P. F., and Tippett J. M. (1992) Tectonic architecture of the mountain front-foreland basin transition, South Island, New Zealand, assessed by fission track analysis. *Tectonics* **11,** 98–113.

Kimbrough D. L., Tulloch A. J., Coombs D. S., Landis C. A., Johnston M. R., and Mattinson J. M. (1994) Uranium-lead zircon ages from the Median Tectonic Zone, New Zealand. *New Zealand J. Geol. Geophys.* **37,** 393–419.

Kirby E., Reiners P. W., Krol M., Hodges K., Farley K. A., Whipple K., Yiping L., Tang W. and Chen Z.(2002) Late Cenozoic uplift and landscape evolution along the eastern margin of the Tibetan plateau: Inferences from $^{40}Ar/^{39}Ar$ and U-Th-He thermochronology. *Tectonics* **10,** 1029/2000TC001246.

Lee J. K. W. and Tromp J. (1995) Self-induced fracture generation in zircon. *J. Geophys. Res.* **100,** 17753–17770.

Lovera O. M., Richter F. M., and Harrison T. M. (1989) The $^{40}Ar/^{39}Ar$ thermochronometry for slowly cooled samples having a distribution of diffusion domain sizes. *J. Geophys. Res.* **94,** 17917–17935.

Lovera O. M., Richter F. M., and Harrison T. M. (1991) Diffusion domains determined by ^{39}Ar released during step heating. *J. Geophys. Res.* **96,** 2057–2069.

Lovera O. M., Grove M., and Harrison T. M. (2002) Systematic analysis of K-feldspar $^{40}Ar/^{39}Ar$ step heating results II: Relevance of laboratory argon diffusion properties to nature. *Geochim. Cosmochim. Acta* **66,** 1237–1255.

Lovera O. M., Grove M., Harrison T. M., and Mahon K. I. (1997) Systematic analysis of K-feldspar $^{40}Ar/^{39}Ar$ step heating results. 1. Significance of activation energy determinations. *Geochim. Cosmochim. Acta* **61,** 3171–3192.

McClelland W. C., Mattinson J. M. (2000) Cretaceous-Tertiary evolution of the western Coast Mountains, central southeastern Alaska. In *Tectonics of the Coast Mountains, Southeastern Alaska and British Columbia* (eds. H. H. Stowell and W. C. McClelland). *Geol. Soc. Am. Spec. Pap.* **343,** pp. 159–182.

McDougall T. and Harrison T. M. (1999) *Geochronology and Thermochronology by the $^{40}Ar/^{39}Ar$ Method,* 2nd ed. Oxford University Press. 269 pp.

Meesters A. G. C. A. and Dunai T. J. (2002) Solving the production-diffusion equation for finite diffusion domains of various shapes Part II. Application to cases with α-ejection and nonhomogeneous distribution of the source. *Chem. Geol.* **186,** 347–363.

Nasdala L., Wenzel M., Vavra G., Irmer G., Wenzel T., and Kober B. (2001) Metamictisation of natural zircon: Accumulation versus thermal annealing of radioactivity-induced damage. *Contrib. Mineral. Petrol.* **141,** 125–144.

Nasdala L., Reiners P. W., Garver J. I., Kennedy A. K., Stern R. A., Balan E. and Wirth R. (2004) Incomplete retention of radiation damage in zircon from Sri Lanka. *Am. Mineral.* **89,** 219–231.

Parrish R. R. (1983) Cenozoic thermal evolution and tectonics of the Coast Mountains of British Columbia 1. Fission track dating, apparent uplift rates, and patterns of uplift. *Tectonics* **2,** 601–631.

Parsons I., Brown W. L., and Smith J. V. (1999) $^{40}Ar/^{39}Ar$ thermochronology using alkali feldspars; real thermal history or mathematical mirage of microtexture? *Contrib. Mineral. Petrol.* **136,** 92–110.

Reddy S. M., Potts G. J., and Kelley S. P. (2001) $^{40}Ar/^{39}Ar$ ages in deformed potassium feldspar: Evidence of microstructural control on Ar isotope systematics. *Contrib. Mineral. Petrol.* **141,** 186–200.

Reiners P. W. and Farley K. A. (1999) He diffusion and (U-Th)/He thermochronometry of titanite. *Geochim. Cosmochim. Acta* **63,** 3845–3859.

Reiners P. W. and Farley K. A. (2001) Influence of crystal size on apatite (U-Th)/He thermochronology: An example from the Bighorn Mountans, Wyoming. *Earth Planet. Sci. Lett.* **188,** 413–420.

Reiners P. W., Farley K. A., and Hickes H. J. (2002a) He diffusion and (U-Th)/He thermochronometry of zircon: Initial results from Fish Canyon Tuff and Gold Butte. *Tectonophys.* **349,** 247–308.

Reiners P. W., Ehlers T. A., Garver J. I., Mitchell S. G., Montgomery D. R., Vance J. A., and Nicolescu S. (2002b) Late Miocene exhumation and uplift of the Washington Cascades. *Geology* **30,** 767–770.

Reiners P. W., Zhou Z., Ehlers T. A., Xu C., Brandon M. T., Donelick R. A., and Nicolescu S. (2003) Post-orogenic evolution of the Dabie Shan, eastern China, from fission-track and (U-Th)/He thermochronology. *Am. J. Sci.* **303,** 489–518.

Richter F. M., Lovera O. M., Harrison T. M., and Copeland P. (1991) Tibetan tectonics from $^{40}Ar/^{39}Ar$ analysis of a single K-feldspar sample. *Earth Planet Sci. Lett.* **105,** 266–278.

Sahama T. G. (1981) Growth strucure in Ceylon zircon. *Bull. Minéral.* **104,** 89–94.

Seward D. (1989) Cenozoic basin histories determined by fission-track dating of basement granites. South Island, New Zealand. *Chem. Geol.* **79,** 31–48.

Smith D. G. W., de St. Jorre L., Reed J. S. B., and Long J. V. P. (1991) Zonally metamictized and other zircons from Thor Lake, Northwest Territories. *Can. Mineral.* **29,** 301–309.

Spanninga G. A. (1993) Evolution of the Grey Valley Trough. M.Sc. thesis, University of Waikato.

Spell T. L., McDougall I., and Tulloch A. J. (2000) Thermochronologic constraints on the breakup of the Pacific Gondwana margin: The Paparoa Metamorphic Core Complex, South Island, New Zealand. *Tectonics* **19,** 433–451.

Staudacher T. H., Jessberger E. K., Dorflinger D., and Kiko J. (1978) A refined ultrahigh-vacuum furnace for rare gas analysis. *J. Phys. E: Sci. Instrum.* **11,** 781–784.

Steven T. A., Mehnert H. H., and Obradovich J. D. (1967) Age of volcanic activity in the San Juan Mountains, Colorado. *U. S. Geol. Surv. Prof. Pap.* **575-D,** 47–55.

Stowell H. H., Crawford M. L. (2000). Metamorphic history of the Coast Mountains orogen, western British Columbia and southeastern Alaska. In *Tectonics of the Coast Mountains, Southeastern Alaska and British Columbia* (eds. H. H. Stowell and W. C. McClelland). *Geol. Soc. Am. Spec. Pap.* **343,** pp. 257–283.

Strutt R. J. (1910a) The accumulation of helium in geologic time, II. *Proc. Roy. Soc. Lond., Ser. A* **83,** 96–99.

Strutt R. J. (1910b) The accumulation of helium in geologic time, III. *Proc. Roy. Soc. Lond., Ser. A* **83,** 298–301.

Strutt R. J. (1910c) Measurements of the rate at which helium is produced in thorianite and pitchblende, with a minimum estimate of their antiquity. *Proc. Roy. Soc. Lond., Ser. A* **83,** 386–388.

Tagami T., Ito H., and Nishimura S. (1990) Thermal annealing characteristics of spontaneous fission tracks in zircon. *Chem. Geol.* **80,** 159–169.

Tagami T., Farley K. A., and Stockli D. F. (2003) (U-Th)/He geochronology of single zircon grains of known Tertiary eruption age. *Earth Planet. Sci. Lett.* **207,** 57–67.

Tagami T., Galbraith R. F., Yamada R. and Laslett G. M.(1998) Revised annealing kinetics of fission tracks in zircon and geological implications. In *Advances in Fission-Track Geochronology* (eds. P. Van den Haute and F. De Corte), pp. 99–112 Kluwer (Dordrecht).

Tulloch A. J. (1988) Batholiths, plutons and suites: Nomenclature for granitoid rocks of Westland-Nelson. *New Zealand J. Geol. Geophys.* **31,** 505–509.

Tulloch A. J. and Kimbrough D. L. (1989) The Paparoa Metamorphic Core Complex, New Zealand: Cretaceous extension associated with fragmentation of the Pacific margin of Gondwana. *Tectonics* **8,** 1217–1234.

Tulloch A. J (2003) U-Pb geochronology of plutonic rocks from Stewart Island New Zealand, Unpublished immediate report, June 2003. Techfile D48/59 xref E48, D49, E49, D50. Institute of Geological and Nuclear Sciences, Dunedin.

Tulloch A. J., Kimbrough D. L., Walker N., and Allibone A. H. (2001) Age relations of New Zealand Paleozoic S-, I, and A-type granite suites, in "S-type granites and related rocks", Alan White Symposium, La Trobe University, Melbourne. AGSO Record 2001/2 p. 95–96.

Villa I. M. (1994) Multipath Ar transport in K-feldspar deduced from isothermal heating experiments. *Earth Planet. Sci. Lett.* **122,** 393–401.

Waight T. E., Weaver S. D., Ireland T. R., Maas R., Muir R. J., and Shelley D. (1997) Field characteristics, petrography, and geochronology of the Hohonu Batholith and the adjacent Granite Hill Complex, North Westland, New Zealand. *New Zealand J. Geol. Geophys.* **40,** 1–17.

Waight T. E., Weaver S. D., and Muir R. J. (1998) Mid-Cretaceous granitic magmatism during the transition from subduction to extension in southern New Zealand: A chemical and tectonic synthesis. *Lithos.* **45,** 469–482.

Watters W., Speden. I. G. and Wood B. L. (1968) Sheet 26-Stewart Island. Geological map of New Zealand. **1,** 250,000. Dept. Sci. Ind. Res., Wellington, New Zealand.

Wendt I. and Carl C. (1991) The statistical distribution of the mean squared weighted deviation. *Chem. Geol.* **86,** 275–285.

Wolf R. A., Farley K. A., and Silver L. T. (1996) Helium diffusion and low-temperature thermochronometry of apatite. *Geochim. Cosmochim. Acta* **60,** 4231–4240.

Wolf R. A., Farley K. A., and Kass D. M. (1998) Modeling of the temperature sensitivity of the apatite (U-Th)/He thermochronometer. *Chem. Geol.* **148,** 105–114.

Wood D. J., Stowell H. H., Onstott T. C., and Hollister L. S. (1991) $^{40}Ar/^{39}Ar$ constraints on the emplacement, uplift and cooling of the Coast plutonic Complex sill, SE Alaska. *Geol. Soc. Am. Bull.* **103,** 849–860.

Yamada R., Tagami T., Nishimura S., and Ito H. (1995) Annealing kinetics of fission tracks in zircon: An experimental study. *Chem. Geol.* **122,** 249–258.

Zaun P. E. and Wagner G. A. (1985) Fission-track stability in zircons under geological conditions. *Nucl. Tracks* **10,** 303–307.

Zeitler P. K., Herczeg A. L., McDougall I., and Honda M. (1987) U-Th-He dating of apatite: A potential thermochronometer. *Geochim. Cosmochim. Acta* **51,** 2865–2868.

Zhang M., Salje E. K. H., Capitani G. C., Leroux H., Clark A. M., Schlüter J., and Ewing R. C. (2000) Annealing of α-decay damage in zircon: A. Raman spectroscopic study. *J. Phys.: Condens. Matter* **12,** 3131–3148.

APPENDIX A

GEOLOGIC AND CHRONOLOGIC CONTEXT OF SAMPLES FOR COMPARISON OF (U-Th)/He AND $^{40}Ar/^{39}Ar$ THERMOCHRONOLOGY

A1. SOUTHWEST ARM GRANITE

The Southwest Arm Granite is located in central Stewart Island, off the southern tip of South Island, New Zealand. Stewart Island is ~60 × 70 km in size and has previously been broadly subdivided into two distinct geologic areas based on reconaissance mapping (Watters et al., 1968). The southwestern two-thirds of the island was originally mapped as undivided Rakehua Granite and Pegasus Group metasedimentary rocks, separated from Anglem Complex plutonic rocks of the northeastern third of the island by greenschist facies volcanic and volcaniclastic rocks of the Paterson Group (Watters et al., 1968; Allibone, 1991). This boundary represents the Median Tectonic Zone, separating rocks of continental basement affinity on the southwest from those intruded and accreted to the Gondwana margin during Paleozoic to Mesozoic convergence on the northeast. Recent detailed mapping (Allibone and Tulloch, 1997) of central and southern Stewart Island has revealed a complex geology which includes several distinctive paragneiss and orthogneiss units and up to 11 intrusive units comprising a range of lithologies from gabbro to granite.

Until recently the tectonothermal history of Stewart Island has received very little attention. Cretaceous Rb/Sr ages of 104 Ma and 97 Ma on muscovite and biotite respectively, were reported by Aronson (1965, 1968) for samples from the southern and central parts of the island. These Rb/Sr ages represent cooling during the same interval of time that crustal extension and metamorphic core complex formation was occurring in western South Island (Tulloch and Kimbrough, 1989; Waight et al., 1997; Spell et al., 2000). U/Pb crystallization ages of 138–146 Ma were reported for igneous and metavolcanic rocks of the Anglem Complex and the Patterson Group (Kimbrough et al., 1994). Gneissic and igneous rocks from central and southern Stewart Island have U/Pb dates ranging from Paleozoic to Cretaceous, but are mostly Cretaceous (Tulloch et al., 2001).

The sample of the Southwest Arm Granite selected for this study was collected from outcrop near the center of the pluton and ~1.5 km west of the Southwest Arm of Patterson Inlet (NZMS series topographic sheet reference D49 176391). Tulloch et al. (2001) have obtained a U/Pb crystallization age of 167 ± 2 Ma (2σ) for this granite. No other previous geochronologic data exist.

A2. TE KINGA MONZOGRANITE

The Te Kinga Monzogranite is part of the Hohonu Batholith, a Paleozoic to Cretaceous plutonic complex exposed west of the Alpine Fault on South Island, New Zealand (Tulloch, 1988). The batholith comprises 10 plutons ranging in age from 381 Ma to 109 Ma, but dominated by mid-Cretaceous granitoids (Waight et al., 1997). Emplacement of the Devonian plutons corresponds to a widespread interval of plutonism present throughout the convergent Gondwana margin in New Zealand, Australia, and Antarctica. Cretaceous plutons were emplaced during a transitional interval from subduction to extension preceding opening of the Tasman Sea in the late Cretaceous (Waight et al., 1998). Unroofing and rapid cooling occurred initially in the mid-Cretaceous in response to continental extension which formed the nearby Paparoa metamorphic core complex (Tulloch and Kimbrough, 1989; Spell et al., 2000). After separation of New Zealand from Australia and Antarctica, the area underwent minor subsidence as indicated by Tertiary sediments lying unconformably on Cretaceous granites in the region, as well as resetting of apatite fission tracks and partial annealing of zircon fission tracks (Seward, 1989; Kamp et al., 1992). A final interval of unroofing occurred beginning in the late Cenozoic as recorded in apatite fission track ages which range from Miocene to Quaternary (Seward, 1989; Kamp et al., 1992; Spaninga, 1993). Waight et al. (1997) summarized the geochronologic data and constructed a *T-t* cooling history for the Hohonu Batholith indicating rapid cooling during the interval ~110–85 Ma immediately after intrusion of Cretaceous plutons at 114–109 Ma, a decrease in cooling rate to nearly isothermal conditions until ~20 Ma indicating a tectonic hiatus and subsidence, and ending with rapid unroofing between ~15–5 Ma associated with convergence on the Alpine Fault.

Previously published geochronologic data on the Te Kinga Monzogranite comprises part of the more regional database discussed above. An ion microprobe $^{238}U/^{206}Pb$ zircon crystallization age of 108.7 ± 3.0 Ma (2σ) gives the timing of intrusion of the pluton (Waight et al., 1997). Muscovite–whole rock and biotite–whole rock Rb/Sr isochron ages of 104.0 ± 2.0 Ma and 73.6 ± 2.0 Ma (2σ), respectively, were also reported by Waight et al. (1997). These Rb/Sr data record cooling during the regional extensional denudation event in the mid-Cretaceous. An apatite fission track age of 5.3 ± 1.0 Ma (2σ) reported by Spanninga (1993) defines unroofing during the most recent convergent tectonism of the Alpine Fault. Together these data indicate a cooling history for the Te Kinga Monzogranite which is consistent with other data from the Hohonu Batholith.

For this study two samples were selected. Sample KFR7, from which the above U/Pb, Rb/Sr, and fission-track were obtained, was collected from near the base of the exposed pluton at 120 m elevation and ~2 km from the Alpine Fault (NZMS series topographic sheet reference K32 849337). Sample TK7 was collected from near the center of the pluton at 1200 m elevation and ~4 km from the Alpine Fault (NZMS series topographic sheet reference K32 867370).

A3. COAST PLUTONIC COMPLEX AT TRACY ARM, HOLKHAM BAY

The Coast Plutonic complex (CPC) of southeast Alaska and British Columbia is a plutonic and metamorphic belt that was active from late Cretaceous through early Tertiary. Crystallization ages of plutons in the northern Coast Mountains part of the CPC are dominantly 55–73 Ma (Crawford et al., 1987; Stowell and Crawford, 2000). Rapid uplift and exhumation of the CPC occurred from about 62–48 Ma, after cessation of subduction and most magmatism, based on P-T-t paths, some of which imply very high geothermal gradients (e.g., 400°C at ~7 km) (Crawford et al., 1987; McClelland and Mattinson, 2000). Both fission-track and (U-Th)/He results suggest that after the early Tertiary orogenic episode of the northern Coast Mountains (e.g., Alaskan part), little exhumation occurred between about 30–10 Ma (Parrish, 1983; Donelick, 1986; Hickes et al., 2000; Hickes, 2000). At some point in the Neogene, 15–10 Ma, exhumation rates increased, exposing samples near sea level, with apatite He ages as young as 6–7 Ma (Hickes et al., 2000; Hickes, 2000). Farley et al. (2001) presented similar results for the Coast Mountains to the south, in British Columbia, although they also invoke a more recent increase in exhumation rates, beginning at 2–4 Ma.

APPENDIX B
ANALYTICAL METHODS FOR AGE DETERMINATIONS

B1. (U-Th)/He DATING

Most zircon (U-Th)/He ages were performed by Nd: YAG laser heating for He extraction, and sector ICP-MS for U-Th determinations, at Yale University. A few samples (8500-15 zircons, titanites, and some of the apatites reported here) were analyzed by either furnace or CO_2 laser heating and quadrupole ICP-MS at Washington State University. Most zircon aliquots comprised single grains (Table 3). Dated crystals were hand-picked from separates with high power (160×) stereo-zoom microscopes with cross-polarization for screening inclusions, although most of these zircon crystals did contain small (~5–20 um) visible inclusions. Selected crystals were measured and digitally photographed in at least two different orientations for α-ejection corrections. Crystals were loaded into 1-mm Pt foil tubes (in some cases, Mo was used for zircon), which were then loaded into copper or stainless steel sample planchets with 20–30 sample slots. Planchets were loaded into a ~10-cm laser cell with sapphire (or ZnS for the CO_2 laser) window, connected by high-vacuum flexhose to the He extraction/measurement line. Once in the laser cell and pumped to $<10^{-7}$–10^{-8} torr, crystal-bearing foil tubes were individually heated using power levels of 1–5 W on the Nd:YAG, or 5–15 W on the CO_2 laser, for 3 min for apatite or 20 min for zircon. Temperatures of heated foil packets were not measured, but from experiments relating luminosity and stepwise degassing of both apatite and zircon, we estimate typical heating temperatures of 1000°C for apatite, and 1250–1400°C for zircon. ^{4}He blanks (0.05–0.1 femtomol ^{4}He, after correction for spike ^{4}He) were determined by heating empty foil packets using the same procedure. Crystals were checked for quantitative degassing of He by sequential reheating. While apatites rarely exhibited residual gas after the first degassing, about 50% of zircons did, and frequently required 2–3 reheatings to reduce the yield to <1–2% of the total gas extracted. Gas liberated from samples was processed by: 1) spiking with ~0.4 pmol of ^{3}He, 2) cyrogenic concentration at 16K on a charcoal trap (condensation time calibrated for no significant ^{4}He/^{3}He fractionation), and purification by release at 37K, and 3) measurement of ^{4}He/^{3}He ratios (corrected for HD and H_3 by monitoring H^+) on a quadrupole mass spectrometer next to a cold Zr-alloy getter. All ratios were referenced to multiple same-day measured ratios and known volumes of ^{4}He standards processed in the same way. Linearity of this standard referencing procedure has been confirmed over four orders of magnitude of ^{4}He intensity. ^{4}He standard reproducibility averages 0.2% on a daily and long-term (tank-depletion corrected) basis. Estimated 2σ analytical uncertainty on sample He determinations, including precision and accuracy from original manometric ^{4}He standard calibrations, is 1–2%.

After degassing, samples were retrieved from the laser cell, spiked with a calibrated ^{229}Th and ^{233}U solution, and dissolved. Apatites were dissolved in situ from Pt tubes in ~30% HNO_3 in Teflon vials. Zircons and titanites were removed from foil and then dissolved in Teflon microvials in Parr bombs with HF and HNO_3, followed by either H_3BO_3 or another bomb run with HCl to remove fluoride salts, and a final dissolution in HNO_3. Each sample batch was prepared with a series of acid blanks and spiked normals to check the purity and calibration of the reagents and spikes. Spiked solutions were analyzed as 0.5 mL of ~1–5 ppb U-Th solutions by isotope dilution on a Finnigan Element2 ICP-MS with a Teflon micro-flow nebulizer and double-pass spray chamber. Routine in-run precisions and long-term reproducibilities of standard ^{232}Th/^{229}Th and ^{238}U/^{233}U are 0.1–0.4%, and uncertainty on sample U-Th contents are estimated to be 1–2% (2σ).

α-ejection was corrected using the method of Farley et al. (1996) and Farley (2002). Replicate analyses of Durango apatite and Fish Canyon Tuff zircon during the period of these analyses yielded mean ages of 32.4 ± 1.5 Ma (2σ, n = 42) and 28.3 ± 2.3 Ma (2σ, n = 63), respectively. On the basis of reproducibility of these and other intralaboratory standards, we estimate an analytical uncertainty of 6% and 8% (2σ) for apatite and zircon, respectively, in this study.

B2. K-FELDSPAR ^{40}Ar/^{39}Ar DATING

Samples from Alaska and the Hohonu Range, New Zealand, were analyzed by the ^{40}Ar/^{39}Ar method at the University of Nevada Las Vegas (UNLV). Samples were wrapped in Al foil and stacked in 6-mm-inside-diameter Pyrex tubes. Neutron fluence monitors (FC-2, Fish Canyon Tuff sanidine) were placed every 5–10 mm along the tube. Synthetic K-glass and optical grade CaF_2 were included to monitor neutron-induced argon interferences from K and Ca. Samples were irradiated for 7–10 h in the D3 position at the Nuclear Science Center at Texas A&M University.

Irradiated crystals together with CaF_2 and K-glass fragments were placed in a Cu sample tray in a high vacuum extraction line and were fused using a 20 W CO_2 laser. Samples analyzed by the furnace step heating method utilized a double vacuum resistance furnace similar to the Staudacher et al. (1978) design. Calibration of the furnace was achieved via a double thermocouple experiment with an internal and external (control) thermocouple. Temperature/time data derived from the internal thermocouple were used for diffusion experiments which were performed in unlined Mo crucibles. Reactive gases were removed by a single MAP and two GP-50 SAES getters before being admitted to a MAP 215-50 mass spectrometer by expansion. Peak intensities were measured using a Balzers electron multiplier by peak hopping through 7 cycles; initial peak heights were determined by linear regression to the time of gas admission. Mass spectrometer discrimination and sensitivity was monitored by repeated analysis of atmospheric argon aliquots from an on-line pipette system.

Measured air argon ^{40}Ar/^{36}Ar ratios were 289.00 ± 0.78 to 290.76 ± 0.47 during this work, thus discrimination corrections of 1.02250 to 1.01630 (4 AMU) were applied to measured isotope ratios. K and Ca correction factors are given in the appropriate data tables for each sample. The sensitivity of the mass spectrometer was $\sim 6 \times 10^{-17}$ mol mV^{-1} with the multiplier operated at a gain of 60 over the Faraday. Line blanks averaged 5.94 mV for mass 40 and 0.02 mV for mass 36 for laser fusion analyses. Blanks for furnace analyses averaged 37.15 mV for mass 40 and 0.12 mV for mass 36 at 600°C and 53.08 mV for mass 40 and 0.17 mV for mass 36 at 1400°C. Computer-automated operation of the sample stage, laser, extraction line, and mass spectrometer as well as final data reduction and age calculations were done using the LabSPEC software written by B. Idleman (Lehigh University). An age of 27.9 Ma (Steven et al., 1967; Cebula et al., 1986) was used for the Fish Canyon Tuff sanidine fluence monitor in calculating ages for samples. An error in J of 0.5% was used in age calculations.

Samples from Stewart Island, New Zealand, were analyzed by the ^{40}Ar/^{39}Ar method at New Mexico Tech. Equipment utilized in the NMT lab is similar to that used at UNLV as described in Heizler et al. (1999).

For ^{40}Ar/^{39}Ar analyses, a plateau segment consists of three or more contiguous gas fractions having analytically indistinguishable ages (i.e., all plateau steps overlap in age at ± 2σ analytical error) and comprising a significant portion of the total gas released (typically >50%). Total gas (integrated) ages are calculated by weighting the amount of ^{39}Ar released, whereas plateau ages are weighted by the inverse of the variance. Inverse isochron diagrams are examined based on the MSWD criteria of Wendt and Carl (1991) and, as for plateaus, must comprise contiguous steps and a significant fraction of the total gas released. K-feldspar thermal modeling follows standard procedures outlined in Lovera et al. (1989, 1991). Conformity of models to the assumptions of the technique was assessed by a correlation coefficient (C_{fg}) between age and log r/r_0 spectra (Lovera et al., 2002), and 90% confidence intervals for K-feldspar cooling histories were calculated using software available at http://oro.ess.ucla.edu/argon.html. All ^{40}Ar/^{39}Ar analytical data are reported at the confidence level of 1σ (standard deviation).

APPENDIX C: $^{40}Ar/^{39}$ Ar DATA

Table C1. Te Kinga Monzogranite, KFR7 muscovite, 4.95* mg, J = 0.001257 ± 0.5% 4 amu discrimination = 1.01848 ± 0.17%, 40/39K = 0.01309 ± 80.0%, 36/37Ca = 0.0002823 ± 1.78%, 39/37Ca = 0.0006949 ± 0.72%.

Step	*T* (°C)	*t* (min)	^{36}Ar	^{37}Ar	^{38}Ar	^{39}Ar	^{40}Ar	%^{40}Ar*	% ^{39}Ar rlsd	Ca/K	^{40}Ar*/^{39}ArK	Age (Ma)	1 s.d.
1	650	12	1.69	0.036	0.425	6.727	720.969	33.2	0.72	0.35	34.358	76.28	0.60
2	725	12	0.81	0.036	0.264	8.848	561.786	61.4	0.95	0.27	37.212	82.47	0.54
3	800	12	1.12	0.047	0.549	25.312	1310.157	76.9	2.71	0.12	39.092	86.54	0.49
4	850	12	1.147	0.045	1.644	107.881	4910.68	93.7	11.53	0.03	42.571	94.04	0.51
5	875	12	0.877	0.045	1.85	130.999	5840.89	96.1	14.00	0.02	42.779	94.49	0.51
6	915	12	0.912	0.047	2.158	151.838	6740.891	96.5	16.23	0.02	42.773	94.48	0.51
7	955	12	0.628	0.05	1.381	95.617	4206.806	96.3	10.22	0.03	42.209	93.27	0.50
8	1010	12	0.443	0.048	0.996	70.097	3044.328	96.7	7.49	0.05	41.712	92.20	0.50
9	1070	12	0.429	0.042	0.887	62.581	2757.98	96.5	6.69	0.04	42.198	93.24	0.50
10	1130	12	0.379	0.051	1.558	115.448	5058.748	98.5	12.34	0.03	42.983	94.93	0.51
11	1180	12	0.28	0.047	1.695	127.928	5630.471	99.2	13.68	0.02	43.505	96.05	0.51
12	1220	12	0.17	0.07	0.358	25.295	1148.592	98.9	2.70	0.18	43.596	96.25	0.52
13	1400	12	0.215	0.167	0.142	6.912	364.329	95.9	0.74	1.60	44.256	97.67	0.56
											Total gas age =	93.94	0.48

Isotope beams in mV; rlsd = released. Error in age includes 0.5% J error; all errors 1σ. (^{36}Ar through ^{40}Ar are measured beam intensities, corrected for decay in age calculations).

Table C2. Te Kinga monzogranite, KFR7 biotite, 5.53 mg, J = 0.001254 ± 0.5% 4 amu discrimination = 1.02090 ± 0.28%, 40/39K = 0.01309 ± 80.0%, 36/37Ca = 0.0002823 ± 1.78%, 39/37Ca = 0.0006949 ± 0.72%.

Step	*T* (°C)	*t* (min)	^{36}Ar	^{37}Ar	^{38}Ar	^{39}Ar	^{40}Ar	% ^{40}Ar*	% ^{39}Ar rlsd	Ca/K	^{40}Ar*/^{39}ArK	Age (Ma)	1 s.d.
1	600	12	7.751	0.083	1.608	12.06	2494.643	10.2	1.78	0.51	20.875	46.62	1.46
2	700	12	1.961	0.116	0.899	39.815	1802.707	70.1	5.88	0.22	31.154	69.14	0.46
3	775	12	1.227	0.101	1.487	94.982	3574.688	90.7	14.03	0.08	33.872	75.05	0.46
4	850	12	1.046	0.115	1.507	100.915	3741.916	92.9	14.90	0.08	34.209	75.78	0.46
5	925	12	1.09	0.129	1.388	92.53	3532.844	92.1	13.66	0.10	34.895	77.27	0.47
6	1005	12	0.973	0.147	1.587	106.964	3805.183	93.6	15.79	0.10	33.058	73.28	0.45
7	1070	12	0.502	0.12	1.49	108.952	3774.014	97.2	16.09	0.08	33.423	74.07	0.45
8	1135	12	0.392	0.151	1.079	76.298	2818.913	97.5	11.27	0.15	35.603	78.80	0.48
9	1220	12	0.374	0.427	0.437	29.206	1188.525	94.4	4.31	1.08	37.204	82.26	0.50
10	1400	12	0.33	0.24	0.26	15.507	647.517	91.9	2.29	1.14	35.858	79.35	0.49
											Total gas age =	75.00	0.42

Isotope beams in mV; rlsd = released. Error in age includes 0.5% J error; all errors 1σ. (^{36}Ar through ^{40}Ar are measured beam intensities, corrected for decay in age calculations).

Table C3. Te Kinga monzogranite, KFR7 K-spar, 9.84 mg, J = 0.001257 ± 0.5% 4 amu discrimination = 1.01899 ± 0.15%, 40/39K = 0.01309 ± 80.0%, 36/37Ca = 0.0002823 ± 1.78%, 39/37Ca = 0.0006949 ± 0.72%.

Step	*T* (°C)	*t* (min)	^{36}Ar	^{37}Ar	^{38}Ar	^{39}Ar	^{40}Ar	% ^{40}Ar*	% ^{39}Ar rlsd	Ca/K	^{40}Ar*/^{39}ArK	Age (Ma)	1 s.d.
1	448	13	7.54	0.039	1.426	1.117	2209.51	1.1	0.1	1.72	21.128	47.29	9.02
2	473	13	0.59	0.038	0.125	1.672	207.756	22.2	0.1	1.12	22.319	49.92	0.73
3	499	13	0.525	0.038	0.134	3.22	298.191	56.7	0.2	0.58	45.645	100.65	0.78
4	525	13	0.452	0.046	0.162	5.293	202.456	44.3	0.3	0.43	13.627	30.64	0.25
5	550	13	0.448	0.049	0.206	9.485	261.251	59.6	0.5	0.25	13.943	31.34	0.22
6	576	13	0.39	0.048	0.283	15.735	254.606	66.1	0.8	0.15	9.048	20.40	0.13
7	627	13	0.713	0.08	0.624	38.124	670.567	73.6	2.0	0.10	12.212	27.48	0.17
8	679	14	0.579	0.096	0.797	53.652	568.839	75.8	2.8	0.09	7.493	16.91	0.10
9	704	14	0.314	0.081	0.587	40.949	294.796	80.0	2.1	0.10	4.995	11.29	0.07
10	730	14	0.296	0.076	0.587	40.419	337.489	84.6	2.1	0.09	6.250	14.12	0.09
11	756	14	0.239	0.077	0.451	31.21	233.445	85.0	1.6	0.12	5.284	11.94	0.08
12	781	14	0.22	0.081	0.44	30.503	231.905	87.7	1.6	0.13	5.538	12.52	0.08
13	807	14	0.204	0.086	0.468	32.738	246.106	90.8	1.7	0.13	5.737	12.96	0.08
14	851	13	0.232	0.111	0.677	47.586	368.036	94.2	2.5	0.11	6.511	14.70	0.09
15	884	13	0.227	0.105	0.673	49.095	391.779	92.7	2.5	0.11	6.663	15.05	0.09
16	935	14	0.313	0.134	1.003	72.187	641.778	91.5	3.7	0.09	7.657	17.28	0.10
17	976	13	0.321	0.119	1.016	72.534	742.478	92.4	3.8	0.08	8.981	20.25	0.12
18	1018	14	0.481	0.117	1.066	74.689	971.25	89.3	3.9	0.08	11.172	25.16	0.14
19	1059	14	0.707	0.113	1.223	83.008	1387.81	87.7	4.3	0.07	14.294	32.13	0.18
20	1089	13	0.881	0.103	1.26	85.104	1722.16	87.2	4.4	0.06	17.290	38.79	0.21
21	1089	24	1.05	0.102	1.361	87.679	1964.29	87.2	4.5	0.06	19.003	42.59	0.23
22	1089	38	1.383	0.113	1.465	91.994	2302.25	85.9	4.8	0.06	20.609	46.14	0.25
23	1089	59	1.671	0.108	1.611	101.13	2757.37	86.6	5.2	0.05	22.594	50.52	0.27
24	1089	89	1.986	0.122	1.839	112.86	3301.15	87.7	5.8	0.05	24.285	54.25	0.29
25	1089	118	2.152	0.127	1.74	101.86	3226.39	87.6	5.3	0.06	25.718	57.40	0.31
26	1115	44	1.012	0.08	0.796	46.209	1567.11	87.1	2.4	0.09	27.739	61.83	0.34
27	1141	29	0.949	0.088	0.716	42.771	1497.93	86.0	2.2	0.10	28.785	64.12	0.35
28	1200	15	1.334	0.115	1.146	68.453	2482.16	85.9	3.5	0.08	30.737	68.39	0.37
29	1250	15	1.708	0.134	1.468	87.506	3227.66	85.8	4.5	0.08	31.348	69.72	0.38
30	1280	15	1.518	0.127	1.244	73.206	2822.51	85.7	3.8	0.09	32.676	72.62	0.40
31	1320	15	2.017	0.18	1.679	100.78	3953.09	86.1	5.2	0.09	33.550	74.52	0.40
32	1350	15	1.796	0.189	1.452	85.635	3383.56	85.8	4.4	0.11	33.542	74.50	0.40
33	1400	15	2.012	0.24	1.566	91.047	3775.97	85.6	4.7	0.13	35.184	78.07	0.42
34	1500	14	2.003	0.197	1.077	53.585	2436.44	77.9	2.8	0.18	35.256	78.23	0.43
											Total gas age =	46.23	0.11

Isotope beams in mV; rlsd = released. Error in age includes 0.5% J error; all errors 1σ. (^{36}Ar through ^{40}Ar are measured beam intensities, corrected for decay in age calculations).

Table C4. TK7 muscovite, 5.11 mg, J = 0.001256 ± 0.5% 4 amu discrimination = 1.01848 ± 0.17%, 40/39K = 0.01309 ± 80.0%, 36/37Ca = 0.0002823 ± 1.78%, 39/37Ca = 0.0006949 ± 0.72%.

Step	*T* (°C)	*t* (min)	^{36}Ar	^{37}Ar	^{38}Ar	^{39}Ar	^{40}Ar	% ^{40}Ar*	% ^{39}Ar rlsd	Ca/K	^{40}Ar*/^{39}Ark	Age (Ma)	1 s.d.
1	650	12	2.167	0.041	0.523	7.653	923.361	32.8	0.8	0.359403	38.581	85.37	0.64
2	750	12	1.328	0.033	0.568	23.141	1375.294	73.5	2.4	0.095659	42.964	94.82	0.56
3	820	12	1.166	0.033	0.862	50.675	2559.954	87.8	5.4	0.043683	43.996	97.03	0.53
4	870	12	1.39	0.032	2.016	134.457	6514.901	94.1	14.2	0.015964	44.857	98.88	0.53
5	900	12	1.083	0.044	1.826	125.507	5991.034	95.2	13.3	0.023516	45.189	99.60	0.54
6	945	12	0.926	0.035	1.483	100.468	4809.599	95	10.6	0.023368	45.325	99.89	0.54
7	1000	12	0.754	0.038	1.281	85.845	4113.687	95.3	9.1	0.029693	45.499	100.26	0.54
8	1070	12	0.723	0.036	1.745	121.994	5801.25	96.8	12.9	0.019795	45.964	101.26	0.54
9	1130	12	0.504	0.035	2.292	168.964	7951.81	98.6	17.9	0.013895	46.332	102.04	0.55
10	1170	12	0.307	0.044	1.474	108.702	5101.058	99	11.5	0.027152	46.244	101.86	0.54
11	1220	12	0.273	0.046	0.236	13.682	705.459	93.8	1.4	0.225538	45.926	101.17	0.55
12	1400	12	0.318	0.042	0.139	5.478	337.871	84.9	0.6	0.514372	45.482	100.22	0.56
											Total gas age =	100.15	0.51

Isotope beams in mV; rlsd = released. Error in age includes 0.5% J error; all errors 1σ. (^{36}Ar through ^{40}Ar are measured beam intensities, corrected for decay in age calculations).

Table C5. Te Kinga pluton, TK7 K-spar, 9.08 mg, J = 0.001256 ± 0.5% 4 amu discrimination = 1.02055 ± 0.06%, 40/39K = 0.01309 ± 80.0%, 36/37Ca = 0.0002823 ± 1.78%, 39/37Ca = 0.0006949 ± 0.72%.

Step	*T* (C)	*t* (min)	^{36}Ar	^{37}Ar	^{38}Ar	^{39}Ar	^{40}Ar	% ^{40}Ar*	% ^{39}Ar rlsd	Ca/K	^{40}Ar*/^{39}ArK	Age (Ma)	1 s.d.
1	448	13	1.482	0.038	0.339	3.803	659.285	37.1	0.19	0.537	60.839	132.84	0.80
2	473	13	0.555	0.031	0.181	6.602	827.129	84.4	0.34	0.252	101.363	216.19	1.08
3	499	13	0.322	0.033	0.179	9.446	328.959	80.9	0.48	0.188	25.059	55.91	0.32
4	525	13	0.278	0.043	0.239	14.623	273.298	81.8	0.75	0.158	13.237	29.75	0.16
5	550	13	0.249	0.04	0.289	18.935	235.275	82.5	0.97	0.114	8.648	19.49	0.11
6	576	13	0.267	0.048	0.334	21.811	249.625	81.2	1.11	0.118	7.927	17.87	0.10
7	627	13	0.451	0.062	0.594	37.98	564.711	82.3	1.94	0.088	11.469	25.80	0.14
8	679	14	0.371	0.066	0.578	38.706	388.975	80	1.98	0.092	7.296	16.46	0.10
9	704	14	0.243	0.058	0.447	31.022	287.163	86.8	1.58	0.100	7.010	15.82	0.09
10	730	14	0.24	0.055	0.393	26.872	281.549	86.8	1.37	0.110	7.917	17.85	0.11
11	756	14	0.179	0.049	0.335	23.54	230.219	92.5	1.20	0.112	7.603	17.15	0.12
12	781	14	0.177	0.056	0.339	23.612	234.495	93	1.21	0.127	7.787	17.56	0.10
13	807	14	0.168	0.047	0.399	27.469	272.832	95.1	1.40	0.092	8.107	18.28	0.10
14	851	14	0.206	0.066	0.618	45.082	455.551	94.6	2.30	0.079	8.760	19.74	0.11
15	884	14	0.242	0.067	0.818	58.086	612.728	91	2.97	0.062	9.024	20.33	0.20
16	935	14	0.234	0.073	0.969	71.753	816.246	96	3.66	0.055	10.433	23.49	0.12
17	976	13	0.27	0.075	1.077	79.577	1049.471	96.2	4.06	0.051	12.219	27.48	0.14
18	1018	14	0.325	0.086	1.507	111.118	1763.09	96.8	5.67	0.042	15.051	33.79	0.17
19	1059	14	0.423	0.083	1.489	106.909	2072.646	95.9	5.46	0.042	18.286	40.97	0.21
20	1089	14	0.527	0.075	1.5	105.84	2493.919	95.4	5.40	0.038	22.181	49.57	0.25
21	1089	24	0.66	0.07	1.341	94.196	2608.297	95.1	4.81	0.040	25.745	57.41	0.29
22	1089	39	0.79	0.072	1.293	88.843	2819.497	95.5	4.54	0.044	29.290	65.18	0.33
23	1089	59	0.965	0.072	1.324	89.303	3198.462	96	4.56	0.043	32.857	72.96	0.37
24	1089	89	1.142	0.073	1.273	78.998	3161.848	96.8	4.03	0.050	36.069	79.93	0.40
25	1089	119	1.232	0.063	0.97	57.629	2540.233	98.1	2.94	0.059	38.220	84.59	0.43
26	1115	44	0.629	0.058	0.544	32.272	1461.991	95.3	1.65	0.097	39.856	88.12	0.45
27	1141	29	0.527	0.055	0.485	29.463	1344.939	94.5	1.50	0.100	40.697	89.94	0.46
28	1200	15	0.654	0.071	0.672	42.031	1962.893	92.4	2.15	0.091	42.337	93.47	0.47
29	1250	15	1.081	0.085	1.121	70.132	3286.736	91.7	3.58	0.065	42.551	93.93	0.47
30	1280	15	1.089	0.08	1.108	69.914	3200.321	91.4	3.57	0.062	41.409	91.47	0.46
31	1320	15	1.365	0.099	1.346	85.401	3888.461	90.8	4.36	0.062	41.048	90.69	0.46
32	1350	15	1.391	0.082	1.47	94.93	4170.363	91.8	4.85	0.046	39.851	88.11	0.47
33	1400	15	1.586	0.055	1.983	133.129	5533.797	92.8	6.80	0.022	38.267	84.69	0.43
34	1500	15	1.572	0.08	1.682	106.589	4472.268	91.1	5.44	0.040	37.838	83.76	0.42
35	1500	30	0.892	0.053	0.458	23.135	1101.772	81.4	1.18	0.123	36.640	81.17	0.41
											Total gas age = 59.42		0.30
											Avg. gas age = 58.91		

Isotope beams in mV; rlsd = released. Error in age includes 0.5% J error; all errors 1σ. (^{36}Ar through ^{40}Ar are measured beam intensities, corrected for decay in age calculations).

Table C6. Southwest Arm Granite, Hornblende, 9.99 g, J = 0.00367969 ± 0.09% 4 amu discrimination = 1.01349 ± 0.14%, 40/39K = 0.02824 ± 0.32%, 36/37Ca = 0.00026 ± 7.69%, 39/37Ca = 0.00065 ± 7.69%.

Step	Temp (°C)	Time (min)	^{40}Ar/^{39}Ar	^{37}Ar/^{39}Ar	^{36}Ar/^{39}Ar ($\times10^{-3}$)	^{39}Ar$_K$ ($\times10^{-15}$ mol)	K/Ca	Cl/K ($\times10^{-3}$)	^{40}Ar* (%)	^{39}Ar (%)	Age (Ma)	±1σ (Ma)
1	750	5.4	135.4	2.508	297.7	0.185	0.20	413.5	35.2	2.1	291.8	7.5
2	850	5.1	29.38	1.561	42.68	0.109	0.33	134.6	57.4	1.2	108.7	4.0
3	950	4.8	26.02	8.591	27.88	0.222	0.059	147.1	70.8	2.5	118.9	1.9
4	990	3.4	27.30	9.652	18.43	0.330	0.053	199.5	82.7	3.7	144.8	1.3
5	1010	3.1	25.67	7.502	10.18	0.895	0.068	210.9	90.4	10.0	148.5	0.7
6	1030	2.9	26.40	6.245	6.292	1.52	0.082	202.1	94.7	17.0	159.36	0.5
7	1050	2.4	26.40	6.083	5.073	1.27	0.084	188.0	96.0	14.2	161.47	0.5
8	1070	5.3	26.67	6.695	6.006	0.790	0.076	172.1	95.2	8.8	161.8	0.7
9	1110	5.5	28.45	7.359	11.39	0.876	0.069	708.4	90.1	9.8	163.3	0.7
10	1150	5.6	26.65	6.749	5.123	1.50	0.076	188.6	96.2	16.7	163.27	0.4
11	1250	6.1	26.74	7.273	4.468	1.21	0.070	195.4	97.0	13.5	165.3	0.5
12	1600	6.3	37.53	6.280	46.57	0.052	0.081	178.7	64.5	0.6	154.6	7.6
										Total gas age =	161.3	0.3
										Plateau age =	163.2	0.7

Table C7. Southwest Arm Granite, K-feldspar, 9.83 mg, J = 0.003667018 ± 0.09% 4 amu discrimination = 1.00799 ± 0.12%, 40/39K = 0.02824 ± 0.32%, 36/37Ca = 0.00026 ± 7.69%, 39/37Ca = 0.00065 ± 7.69%.

Step	Temp (°C)	Time (min)	$^{40}Ar/^{39}Ar$	$^{37}Ar/^{39}Ar$	$^{36}Ar/^{39}Ar$ ($\times10^{-3}$)	$^{39}Ar_K$ ($\times10^{-15}$ mol)	K/Ca	Cl/K ($\times10^{-3}$)	$^{40}Ar^*$ (%)	^{39}Ar (%)	Age (Ma)	$\pm1\sigma$ (Ma)
1	500	8.0	42.06	0.0060	50.54	6.89	84.5	19.2	64.4	1.7	170.9	1.4
2	500	14.4	14.85	0.0004	8.394	4.24	1192.6	4.4	83.1	1.0	79.84	0.61
3	550	9.0	14.21	0.0017	4.867	7.31	300.8	4.9	89.7	1.8	82.40	0.38
4	550	14.2	13.59	0.0009	3.150	5.63	557.8	4.1	92.9	1.4	81.67	0.40
5	600	8.6	13.79	0.0029	1.866	7.37	177.2	4.7	95.8	1.8	85.33	0.35
6	600	14.8	13.35	0.0029	1.003	7.21	178.3	4.1	97.6	1.8	84.20	0.33
7	650	9.6	13.53	0.0032	0.9595	11.8	161.9	4.2	97.7	2.9	85.37	0.35
8	650	14.5	13.25	0.0023	0.5741	10.4	222.5	3.7	98.5	2.5	84.32	0.33
9	700	9.8	13.30	0.0026	0.5962	16.2	197.4	3.8	98.5	4.0	84.59	0.31
10	700	14.8	13.14	0.0023	0.4105	12.3	222.3	3.7	98.9	3.0	83.93	0.29
11	750	9.8	13.31	0.0034	0.4988	13.2	149.0	3.7	98.7	3.3	84.87	0.30
12	800	9.7	13.42	0.0104	0.8151	12.7	49.0	4.0	98.0	3.1	84.97	0.31
13	850	9.6	13.46	0.0128	0.9949	8.86	39.9	4.1	97.6	2.2	84.88	0.32
14	900	9.8	13.55	0.0155	1.372	9.02	33.0	4.4	96.8	2.2	84.73	0.39
15	950	9.8	13.90	0.0100	2.226	9.70	51.0	4.5	95.1	2.4	85.39	0.33
16	1000	6.2	14.82	0.0095	3.641	8.73	53.9	4.7	92.6	2.1	88.53	0.42
17	1050	7.0	15.84	0.0071	5.004	19.7	71.9	5.2	90.5	4.8	92.43	0.48
18	1100	9.7	15.81	0.0056	4.674	19.4	91.7	23.0	91.1	4.8	92.83	0.38
19	1100	30.1	15.78	0.0039	4.117	21.5	130.1	5.4	92.1	5.3	93.68	0.37
20	1100	59.7	15.94	0.0026	4.474	17.0	199.4	5.6	91.5	4.2	94.02	0.45
21	1100	119.7	16.43	0.0020	5.119	22.7	255.8	5.3	90.6	5.6	95.88	0.42
22	1100	239.9	16.86	0.0018	6.245	25.9	286.6	5.2	88.9	6.4	96.49	0.39
23	1100	479.7	17.45	0.0017	7.648	28.8	303.0	5.3	86.9	7.1	97.63	0.45
24	1200	9.5	16.74	0.0010	4.825	16.7	491.4	5.4	91.3	4.1	98.42	0.44
25	1300	10.4	16.55	0.0006	4.153	69.0	868.4	5.3	92.4	17.0	98.47	0.53
26	1400	10.5	16.56	0.0020	3.872	6.47	257.8	5.6	92.9	1.6	99.03	0.43
27	1500	10.4	16.58	0.0027	3.993	8.47	187.3	5.3	92.7	2.1	98.91	0.45
										Total gas age =		

Table C8. Tracy Arm/Holkham Bay, 519, K-feldspar, 18.01 mg, J = 0.0007502 ± 0.5% 4 amu discrimination = 1.02250 ± 0.27%, 40/39K = 0.0002 ± 150%, 36/37Ca = 0.0002679 ± 2.52%, 39/37Ca = 0.0007166 ± 4.77%.

Step	*T* (°C)	*t* (min)	^{36}Ar	^{37}Ar	^{38}Ar	^{39}Ar	^{40}Ar	% ^{40}Ar*	% ^{39}Ar rlsd	Ca/K	^{40}Ar*/^{39}ArK	Age (Ma)	1 s.d.
1	447	18	2.867	0.047	0.564	1.89	989.909	16.4	0.07	0.282	85.349	111.97	2.20
2	473	18	1.07	0.056	0.242	2.101	433.647	29.2	0.07	0.302	59.238	78.44	0.93
3	473	43	0.57	0.051	0.135	2.481	247.387	37.1	0.09	0.233	33.216	44.40	0.99
4	514	18	1.089	0.108	0.262	4.005	517.343	39.8	0.14	0.305	50.703	67.35	0.79
5	514	43	0.582	0.162	0.157	4.856	340.338	54.7	0.17	0.378	35.497	47.41	0.54
6	555	18	0.714	0.125	0.212	6.374	467.285	56.8	0.23	0.222	41.060	54.73	0.41
7	555	43	0.427	0.127	0.204	8.671	445.194	76.7	0.31	0.166	37.222	49.69	0.39
8	596	18	0.633	0.132	0.279	10.78	626.886	71.8	0.38	0.139	41.338	55.10	0.39
9	596	43	0.334	0.153	0.261	14.781	648.023	88.7	0.52	0.117	37.453	49.99	0.34
10	637	18	0.309	0.149	0.274	15.926	685.266	88.1	0.57	0.106	37.575	50.15	0.32
11	637	43	0.276	0.154	0.363	24.074	982.997	94.4	0.86	0.072	37.676	50.28	0.34
12	678	19	0.235	0.127	0.345	23.855	970.187	93.8	0.85	0.060	37.987	50.69	0.31
13	678	44	0.208	0.131	0.499	36.35	1438.53	97.6	1.29	0.041	38.087	50.83	0.32
14	719	19	0.249	0.126	0.528	35.786	1432.93	95.6	1.27	0.040	38.202	50.98	0.31
15	719	44	0.177	0.128	0.738	53.156	2064.98	98.8	1.89	0.027	38.057	50.79	0.31
16	760	19	0.127	0.094	0.642	46.484	1801.81	98.4	1.65	0.023	38.146	50.90	0.31
17	760	44	0.184	0.11	0.939	72.03	2831.96	99	2.56	0.017	38.755	51.70	0.31
18	801	19	0.153	0.081	0.767	57.959	2253.81	98.5	2.06	0.016	38.342	51.16	0.31
19	842	19	0.216	0.113	1.258	95.637	3725.24	98.6	3.40	0.013	38.504	51.37	0.31
20	884	19	0.284	0.114	1.745	131.667	5130.06	98.6	4.68	0.010	38.539	51.42	0.31
21	909	19	0.252	0.089	1.7	128.484	4996.73	98.8	4.56	0.008	38.523	51.40	0.31
22	935	19	0.237	0.095	1.645	126.414	4944.41	98.8	4.49	0.009	38.772	51.73	0.32
23	961	19	0.281	0.081	1.648	121.471	4773.84	98.5	4.31	0.008	38.834	51.81	0.32
24	976	19	0.261	0.082	1.33	100.296	3945.57	98.4	3.56	0.009	38.767	51.72	0.31
25	1002	19	0.332	0.082	1.39	100.458	3995.42	97.9	3.57	0.009	38.997	52.02	0.32
26	1017	19	0.297	0.088	1.137	83.547	3335.58	97.8	2.97	0.012	39.077	52.13	0.31
27	1032	19	0.301	0.084	0.993	71.897	2892.6	97.4	2.55	0.013	39.202	52.29	0.32
28	1048	19	0.302	0.086	0.866	63.319	2579.22	97	2.25	0.015	39.536	52.73	0.32
29	1063	19	0.313	0.092	0.777	56.394	2311.57	96.6	2.00	0.018	39.564	52.77	0.32
30	1074	19	0.316	0.082	0.646	47.063	1942.19	95.9	1.67	0.020	39.504	52.69	0.32
31	1084	19	0.287	0.086	0.59	40.7	1685.25	95.7	1.45	0.024	39.544	52.74	0.32
32	1089	24	0.34	0.085	0.591	40.317	1686.2	95	1.43	0.024	39.546	52.74	0.32
33	1089	29	0.301	0.085	0.509	35.747	1496.98	95.3	1.27	0.027	39.583	52.79	0.33
34	1089	39	0.372	0.083	0.521	35.654	1505.33	94.5	1.27	0.026	39.390	52.54	0.32
35	1089	59	0.477	0.09	0.602	39.553	1695.4	94.1	1.40	0.026	39.577	52.78	0.33
36	1089	74	0.485	0.082	0.554	36.87	1600.94	94.1	1.31	0.025	39.769	53.04	0.33
37	1089	74	0.443	0.072	0.471	29.246	1289.63	93.6	1.04	0.028	39.858	53.15	0.32
38	1089	74	0.41	0.059	0.381	24.772	1095.9	93.4	0.88	0.027	39.585	52.80	0.32
39	1089	74	0.365	0.06	0.332	20.806	932.608	93.6	0.74	0.033	39.873	53.17	0.33
40	1089	89	0.403	0.062	0.362	21.067	952.326	95.7	0.75	0.033	40.675	54.23	0.33
41	1089	119	0.484	0.054	0.4	23.819	1088.06	94.1	0.85	0.026	39.949	53.27	0.33
42	1089	149	0.547	0.061	0.448	25.787	1180.43	94.7	0.92	0.027	39.760	53.03	0.32
43	1140	19	0.222	0.052	0.166	10.15	469.836	89.7	0.36	0.058	40.410	53.88	0.36
44	1200	15	0.494	0.075	0.393	22.069	1047.4	87.6	0.78	0.038	41.331	55.09	0.35
45	1230	15	0.756	0.093	0.604	35.427	1680.24	87.8	1.26	0.030	41.548	55.37	0.35
46	1255	15	1.125	0.086	0.917	54.334	2506.73	87.5	1.93	0.018	40.400	53.87	0.34
47	1300	15	3.236	0.109	3.144	197.945	8804.59	89.5	7.03	0.006	39.959	53.29	0.33
48	1350	15	6.276	0.173	7.168	459.308	20066.1	91	16.31	0.004	39.937	53.26	0.33
49	1400	15	1.746	0.044	1.667	107.217	4783.76	89.8	3.81	0.005	40.142	53.53	0.34
50	1500	15	0.23	0.038	0.122	6.646	330.093	84.8	0.24	0.065	40.542	54.05	0.36
						Cumulative % ^{39}Ar rlsd = 100.00					Total gas age = 52.48	0.26	